Tornado Heading and Speed Changes Associated with Large and Intense Internal Rear-Flank Surges in Three Supercells

BRUCE D. LEE[a] AND CATHERINE A. FINLEY[a]

[a] *Department of Atmospheric Sciences, University of North Dakota, Grand Forks, North Dakota*

(Manuscript received 26 October 2021, in final form 20 March 2022)

ABSTRACT: Tornado motion changes occurring with major internal rear-flank momentum surges are examined in three significant tornado-producing supercells. The analysis primarily uses fixed-site Doppler radar data, but also utilizes in situ and videographic observations when available. In the cases examined, the peak lowest-level remotely sensed or in situ rear-flank surge wind speeds ranged from 48 to at least 63 m s^{-1}. Contemporaneous with major surges impacting the tornadoes and their parent low-level mesocyclones, longer-duration tornado heading changes were leftward and ranged from 30° to 55°. In all cases, the tornado speed increased substantially upon surge impact, with tornado speeds approximately doubling in two of the events. A storm-relative change in the hook echo orientation accompanied the major surges and provided a signal that a marked leftward heading change for an ongoing tornado was under way. Concurrent with the surge interaction, the hook echo tip and associated low-level mesocyclone turned leftward while also moving in a storm-relative downshear direction. The major rear-flank internal surges influenced tornado motion such that a generally favorable storm updraft-relative position was maintained. In all cases, the tornado lasted well beyond (≥21 min) the time of the surge-associated left turn with no evident marked loss of intensity until well down-track of the turn. The local momentum balance between outflow and inflow that bounds the tornado or its parent circulation, especially the directionality evolution of the bounding momentum, is the most apparent explanation for tornado down-track or off-track accelerations in the featured events.

KEYWORDS: Supercells; Tornadoes; Radars/Radar observations; Nowcasting

1. Introduction

a. Motivation

The lion's share of tornado research to date has been understandably focused on the tornadogenesis problem (e.g., Brandes 1978; Klemp and Rotunno 1983; Wicker and Wilhelmson 1995; Davies-Jones and Brooks 1993; Markowski and Richardson 2009, 2014; Markowski et al. 2012; Coffer and Parker 2017). A much smaller subset of studies has focused, at least in part, on tornado maintenance or aspects of tornado evolution after development. The research presented here falls into this latter group and is motivated by the lack of guidance on tornado heading (i.e., the direction the tornado is moving) and speed changes post genesis. We are interested in marked changes to tornado motion through the mature stage, but prior to entering the dissipation stage. Understanding associations between evolving supercell flow fields and changes in tornado motion is most actionable and valuable for longer-duration events (i.e., tornado motion changes lasting more than a few minutes). The Greensburg, Kansas, EF5 tornado of 4 May 2007 (Lemon and Umscheid 2008) is an ideal example of where the timely recognition of a tornado-track change by the National Weather Service (NWS) was likely crucial in minimizing casualties by communicating the heightened probability of a direct hit on Greensburg.[1] Even a few minutes lead time of a tornado motion change, or at least the knowledge that a tornado may be entering a period of heightened probability of a motion change, could yield life-saving benefits.

A recent paper by Nixon and Allen (2021) makes the case for operational nowcasting improvements needed to deal with deviant tornado motion. Of the 102 tornadic cases they analyzed where leftward deviant motion was identified through low-level mesocyclone (LLM) tracking at the lowest radar tilt, once the circulation deviated, the LLM moved completely out of the NWS tornado warning polygon in ~25% of the events, thus requiring one or more corrections. Combined with the cases where the LLM moved into the left/rear quarter of the warning polygon (see their Fig. 5 and related details), ~59% of the events moved into or passed through a lower-probability region of the warning area. Over about the last 15 years, we have recognized a pattern where particularly strong internal surges within a tornadic supercell's rear flank (RF) were temporally associated with marked tornado track changes, most usually leftward. Of particular interest are those cases where a tornado leftward turn was not concurrent with dissipation, a period when left turns frequently occur (e.g., Burgess et al. 1982; Dowell and Bluestein 2002, hereafter DB02). This perceived RF internal surge (RFIS) and tornado motion change relationship coupled with an operational need for improved anticipation and recognition of tornado motion changes prompted an examination of several cases where one or more intense RFISs were temporally associated with a marked leftward tornado heading change. Our primary objectives involve gaining a better understanding of this pattern to improve operational radar-based anticipation of potential large leftward tornado track changes while also examining the impact these major surges have on tornado speed. In addition to

[1] Umscheid (2007) provides an illuminating account of the Greensburg tornado tracking and warning evolution from the perspective of the NWS meteorologist in charge of radar operations and warnings.

Corresponding author: Bruce D. Lee, bruce.lee@und.edu

DOI: 10.1175/WAF-D-21-0174.1

benefiting down-track residents, improved recognition of when an ongoing tornado might undergo a marked track and/or speed change would benefit storm researchers and the large contingent of storm observers often present nearby.

Three events of substantial track length and duration were selected for in-depth analysis that highlight contemporaneous tornado heading and speed changes with major RFISs. The first of these involved the large EF2 Quinter, Kansas, tornado of 23 May 2008 (the first of two "Quinter tornadoes" on this date; *Storm Data*, NCDC 2008). The second case featured the record-width 31 May 2013 El Reno, Oklahoma, EF3 tornado (*Storm Data*, NCDC 2013; Bluestein et al. 2015). The final case involved another large tornado, the EF2 Hillsboro, North Dakota, tornado of 11 July 2017 (*Storm Data*, NCDC 2017). Details and analysis of all three cases are presented in section 3.

b. Background

Research has generally attributed tornado motion changes to just a few contributory mechanisms. Some studies ascribe tornado track changes to rotational characteristics of the parent circulation or to vortex interactions. For example, Agee et al. (1976) credited track changes to a multiple-vortex tornado cyclone structure where tornado motion was influenced by its parent circulation. Wakimoto et al. (2003) were able to confirm trochoidal nonlinear tornado motion patterns as a non-centered tornado revolved around its parent mesocyclone. In a few documented cases, tornado track changes were associated with interacting tornadoes (Fujita 1992; Davies-Jones et al. 1994; French et al. 2015). Vortex interaction likely played a role in the track of the east member of the simultaneously occurring twin EF4 tornadoes near Pilger, Nebraska, on 16 June 2014 (https://www.weather.gov/oax/event_archive_20140616) and in a pair of merging quasi-linear convective system tornadoes in Skow and Cogil (2017).

In the last two decades a mechanism frequently cited for causing tornado motion change was presented by DB02 who used airborne Doppler radar data to analyze the evolution and movement of the parent circulations of three significant tornadoes on 8 June 1995 near McLean, Texas. They found that updraft-relative changes in tornado motion were due to changes in the balance between storm outflow and the low-level inflow. When storm outflow weakened, tornadoes gradually became decoupled from the rear portion of the main-storm updraft, a region of favorable tornado maintenance. Westward updraft-relative advection of the tornado by penetrating southeasterly inflow moved the tornadoes farther from this tornado maintenance region leading to tornado dissipation. The marked leftward heading change of tornado 1 in DB02 (their Fig. 14) clearly shows this track evolution.

Related to the DB02 conceptual model, other research has attributed tornado motion deviations with changes in the tornado-proximate flow field. In a study utilizing both mobile and fixed Doppler radar, Tanamachi et al. (2012) suggest occlusion-related flow field changes may have been responsible for tornado leftward and/or rearward updraft-relative motion during the shorter-track cyclic mode of the aforementioned Greensburg tornadic supercell. Lee et al. (2012) documented a leftward and rearward track change of the 22 May 2010 Bowdle, South Dakota, EF4 tornado during the dissipation stage that coincided with a kinematically strong and markedly negatively buoyant RFIS. Expansion of the surge bounding the tornado to the south and east was recognized as a likely cause. Using mobile dual-Doppler wind synthesis and ensemble Kalman filter analyses, Marquis et al. (2012) found that tornado motion deviations were influenced by marked changes in the RF flow field. French et al. (2014) used mobile Doppler radar analysis to attribute two cases of rightward tornado motion to a strengthening of the RF flow field the tornadoes were embedded in. In a polarimetric Doppler radar analysis of the 20 May 2013 Moore, Oklahoma, EF5 tornado event, Kurdzo et al. (2015) made a compelling case that changes in the tornado-proximate outflow–inflow balance by RFISs were instrumental in the tornado executing a track loop while also influencing tornado speed. Nixon and Allen (2021) applied the DB02 conceptual model to create a hodograph-based technique for anticipating leftward tornado deviant motion. Perhaps the most complex process posited in a major tornado track change was by Magsig and Austin (2014) who suggested that the unusual motion of the 31 May 2013 El Reno tornado may have been associated with feedbacks between the large tornado, an expanding strong RF downdraft (RFD) and intensifying larger-scale mesocyclone. While much of the tornado heading-change research involves a tornado entering into, or residing in, the dissipation stage, the cases examined herein involve marked tornado heading changes occurring well before the dissipation stage.

Momentum surges within the RF outflow of supercells that we refer to as RFISs, are also called RFD internal surges or internal RF momentum surges, and are associated with secondary gust fronts behind the main RF gust front (RFGF). These surges have received much attention since the mid-2000s, especially after Finley and Lee (2004), Lee et al. (2004) and Wurman et al. (2007) focused attention on the phenomenon with respect to associations with tornado development or intensification. However, documentation of this phenomenon can be sporadically found decades earlier (e.g., Jensen et al. 1983). As the title implies, these are marked kinematic surges within the RF outflow of supercells, but they often have a distinct thermodynamic signal (e.g., Finley and Lee 2004, 2008; Lee et al. 2004, 2010, 2011, 2012; Hirth et al. 2008; Skinner et al. 2011, 2014; Riganti and Houston 2017). The reader is referred to Skinner et al. (2014, 2015) and Schenkman et al. (2016) for reviews of historical RFIS documentation, including RFISs within simulated supercells, and discussions of surge-related forcing mechanisms informed from their research. Investigating the dynamical relationship between RFISs and tornado motion changes is beyond the scope of this paper; however, in the last section we discuss physical relationships where apparent. In the next section we describe project methodology, followed by three case study analyses, and finally, a summary and discussion of salient points.

2. Methodology

The main source of data utilized in this study is from the Weather Surveillance Radar-1988 Doppler (WSR-88D) network sites at Goodland, Kansas (KGLD); Twin Lakes, Oklahoma

(KTLX); and Mayville, North Dakota (KMVX). Data from the S-band Multifunction Phased Array Radar (MPAR; Zrnić et al. 2007; Heinselman et al. 2008; Weadon et al. 2009; Heinselman and Torres 2011) that was located at the National Weather Radar Testbed in Norman, Oklahoma, were utilized in the analysis of the El Reno event to temporally augment the KTLX radar coverage given its ~71-s update interval. Some prominent constraints of radar data include scan update interval, resolution dependence on distance, and increasing beam height above ground level (AGL) with distance. The radar beam angle orientation with respect to the flow field motion within the RFIS can be a substantial constraint in assessing surge intensity and evolution. For the Hillsboro event analysis, the availability of Supplemental Adaptive Intravolume Low-Level Scans (SAILS; Chrisman 2013, 2014) substantially improved the frequency of lowest-level products (~2 min). Gibson Ridge Level II Analyst software (http://www.grlevelx.com/grlevel2) was utilized to display and analyze the Level II WSR-88D data.

Mobile mesonet data from the Tactical Weather-Instrumented Sampling in/near Tornadoes Experiment (TWISTEX; Karstens et al. 2010) were used in the analysis of the Quinter event. Mesonet data provided near-surface kinematic and thermodynamic attributes of the supercell RF outflow. General details of the TWISTEX mobile mesonet in 2008, data attributes and quality control can be found in Lee et al. (2011). For the Quinter event the nearest radar (KGLD) was located ~130 km from the hook echo resulting in inadequate sampling the RF outflow due to beam-height constraints.

Videography was utilized, sometimes extensively, in all three cases for analysis of tornado, RF outflow, or LLM evolution. In the Quinter event, TWISTEX mesonet teams along with two well-positioned contributing storm chasers documented supercell and tornado evolution. For the El Reno case, synchronized field videography from numerous storm chasers was examined using the Tornado Environment Display (TED; Seimon et al. 2016). Within TED, multiple visual perspectives can be simultaneously viewed while overlaid on updating MPAR lowest-level reflectivity or radial velocity imagery. Videography by the lead author was used in the Hillsboro event analysis.

To see if a temporal association existed between marked tornado heading changes and the presence of a major RFIS, strong surges were identified in the observations. For the El Reno and Hillsboro events where the 0.5° radar beam height was under 1 km above radar level (ARL), the radial velocity was analyzed for RFIS signatures that included a rapidly intensifying flow region with time continuity within the broader RF outflow and a region of high-velocity gradient near the surge leading edge [delineating the RFIS boundary (RFISB)]. Note that the RFISs receiving focused attention in each event were large and intense with evidence of low-level ground-relative winds within the surges of at least 48 m s^{-1}. Based on observational research that documented peak wind speeds within RFISs (e.g., Lee et al. 2011, 2012; Skinner et al. 2014; Kurdzo et al. 2015), these are considered high-end surges. Substantially weaker surges, often present within evolving RF flow fields, were surmised to have a commensurately lower association with marked tornado heading and speed changes. In the El Reno and Hillsboro events, the radars had azimuthally advantageous viewing angles of the surges. Areas of radial wind maxima and accompanying leading-edge velocity gradients were readily detected and tracked. In the Quinter event, the presence of an intense RFIS was observed by the TWISTEX mobile mesonet within the broader RF outflow via velocity and velocity gradient data. Mesonet thermodynamic sampling of this surge revealed a strong signal.

In the selected cases, a track-relative timeline was available or could be created based largely on nearby radar that either resolved the tornado or confirmed its position via tornadic debris signature (TDS; Ryzhkov et al. 2005; Kumjian and Ryzhkov 2008), or videography. A timeline accompanying the track was important for temporally associating tornado heading and speed changes with RFIS impacts. Radar coverage varied from being sufficiently close to resolve both the RFISs and featured tornado (El Reno, Hillsboro), to being only adequate to resolve the tornado parent circulation and hook echo (Quinter) reflective of operational variability.[2] Tornado position chronology was especially important in assessing RFIS influence on tornado speed. For the El Reno event, estimated tornado center locations at 1-min intervals based on University of Oklahoma's rapid-scan X-band polarimetric radar (RaXPol; Pazmany et al. 2013) and KTLX as presented in NOAA (2014) were used in calculating a tornado speed time series. In the Hillsboro case, close tornado proximity to KMVX over much of the analysis period combined with the radar operating in a SAILS mode provided the spatial and temporal resolution to produce a tornado speed time series. In the Quinter event, estimate of the primary tornado's speed is coarser due to the constraints of using 4.5-min KGLD tornadic vortex signature (TVS) data at considerable distance. More case-specific details influencing the quality of the tornado track and confidence in the chronology are presented in section 3.

3. Case studies

a. 23 May 2008 Quinter, Kansas, tornado

1) EVENT OVERVIEW

On the afternoon and evening of 23 May 2008, a tornado outbreak occurred mainly over the western half of Kansas (*Storm Data*, NCDC 2008; Umscheid and Hutton 2008). The first of two tornadic supercells to pass over or near Quinter, designated the Quinter supercell (QS), produced at least five tornadoes between 2100 and 2300 UTC. The track of the most significant tornado associated with the QS is the focus of this subsection. This EF2 tornado (Fig. 1) referred to as the Quinter tornado (QT) developed at about 2143 UTC 4.5 km northwest of Quinter (Fig. 2) and had a 1.6-km peak width, 23-km pathlength, and 30-min duration.

Of interest to this study was an abrupt tornado track change that occurred in conjunction with a large and very intense RFIS (Finley and Lee 2008). The tornado turned markedly to

[2] The El Reno and Hillsboro tornadoes were sufficiently wide to be resolved to an appreciable degree for much of their respective life-spans at the analyzed scanning distances.

FIG. 1. The expansive QT at 2145 UTC looking north (image courtesy of C. Collura).

the left with respect to both its initial path and the tracks of two tornadoes that just preceded it. *Storm Data* (NCDC 2008) mentions RFD winds as a contributing component in damaging 8 km of utility poles. The TWISTEX mobile mesonet measured a 48 m s^{-1} 3 m AGL wind gust associated with this surge. The authors who were directing the TWISTEX mobile mesonet witnessed a row of utility poles at their general location falling with this peak wind.

2) TORNADO TRACKS

Tornado tracks are presented in Fig. 2 to examine the track change for the QT (track C) and the tornado heading change between the QT cycle and those preceding it. Tracks were created utilizing NWS damage survey tracks, mobile radar data presented in Wurman and Kosiba (2013), videography from TWISTEX and two contributing observers, and the TWISTEX damage survey. KGLD TVS guidance was used as a spatial consistency check for the QT that possessed a deep TVS soon after development.[3] The two tornadoes that preceded the QT were not as wide nor long lived, but in the case of the first tornado shown in Fig. 2 (track A), still significant with an approximate 18-min duration, 400-m maximum width (*Storm Data*, NCDC 2008) and strong intensity (Wurman and Kosiba 2013). The mean heading of these tornadoes was about 33° compared to the QT heading of 3° over the first ~5 km beyond the major early turn. The QT maintained a generally northward course well beyond this point. While this 30° tornado heading change between cycles was substantial, it is notable that the QT experienced an early track change of ~40° coincident with the major RFIS noted in the event overview. TWISTEX observed this surge rapidly advecting the small second tornado in Fig. 2 (track B) to the northeast while disrupting its circulation leading to rapid demise.

3) HOOK ECHO AND RF EVOLUTION WITH QT MOTION CHANGES

The QS evolution was analyzed focusing primarily on the hook echo and RF outflow evolution leading up to and during

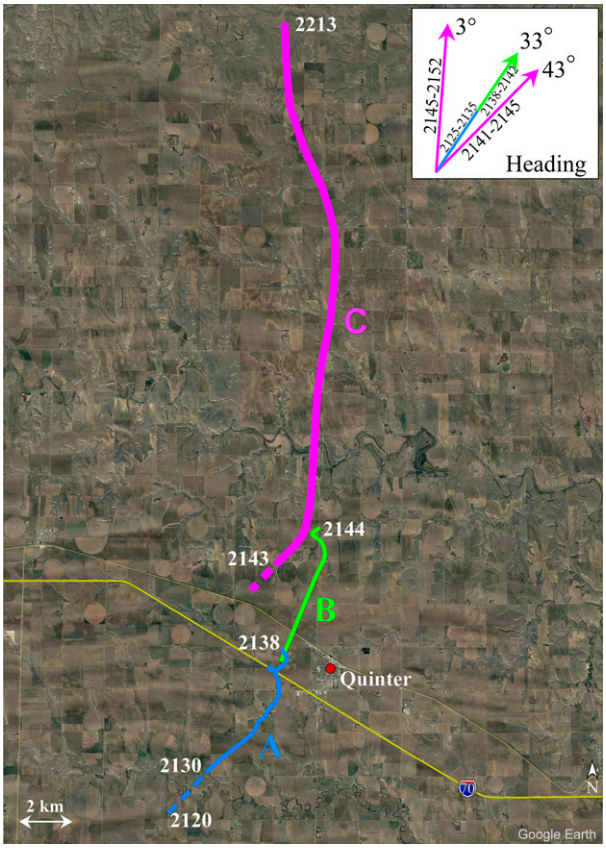

FIG. 2. Tornado tracks for the QT (track C) and the two tornadoes preceding it (tracks A, B). Line widths differentiate the very wide QT from the much narrower prior tornadoes, but do not represent actual damage path width. The dashed segments indicate early track periods having reduced locational confidence. Note that the end of the first tornado and beginning of the second occur near 2138 UTC. The inset shows a clockwise depiction of the QT mean heading for the first ~5 km after the early turn, the mean heading for preceding tornadoes, and the approximate QT early-stage heading. Heading times (UTC) for QT track segments and those used in the mean heading for prior tornadoes are indicated on the heading vectors. The yellow line is Interstate Highway 70.

the major RFIS and large tornado turn. As depicted in Figs. 3 and 4 , the QS flourished during this period as evidenced by a high-reflectivity core with "flying eagle" structure (Kumjian and Schenkman 2008), the development of a prominent hook, and strong mesocyclone. Note that 7.62-cm hail was reported at about the time of Fig. 3a (*Storm Data,* NCDC 2008) and observed again approximately 12 min later by TWISTEX.

Changes in the QS hook echo and RF outflow provide important insights into tornado track evolution. Concurrent with the development of a well-defined hook echo, a visually impressive tornado was in progress during TWISTEX initial deployment (Fig. 2 first tornado, Fig. 3a). As the hook echo acquired more definition by 2136 UTC (Fig. 3b) the first major tornado cycle ended (2138 UTC) and next tornado cycle began (Fig. 2, second tornado). What happens next with the hook echo provides a potentially important signal that a major

[3] Even at ~130 km from KGLD, a tight radial velocity couplet of similar diameter to the tornado damage track width extended above 4000 m ARL.

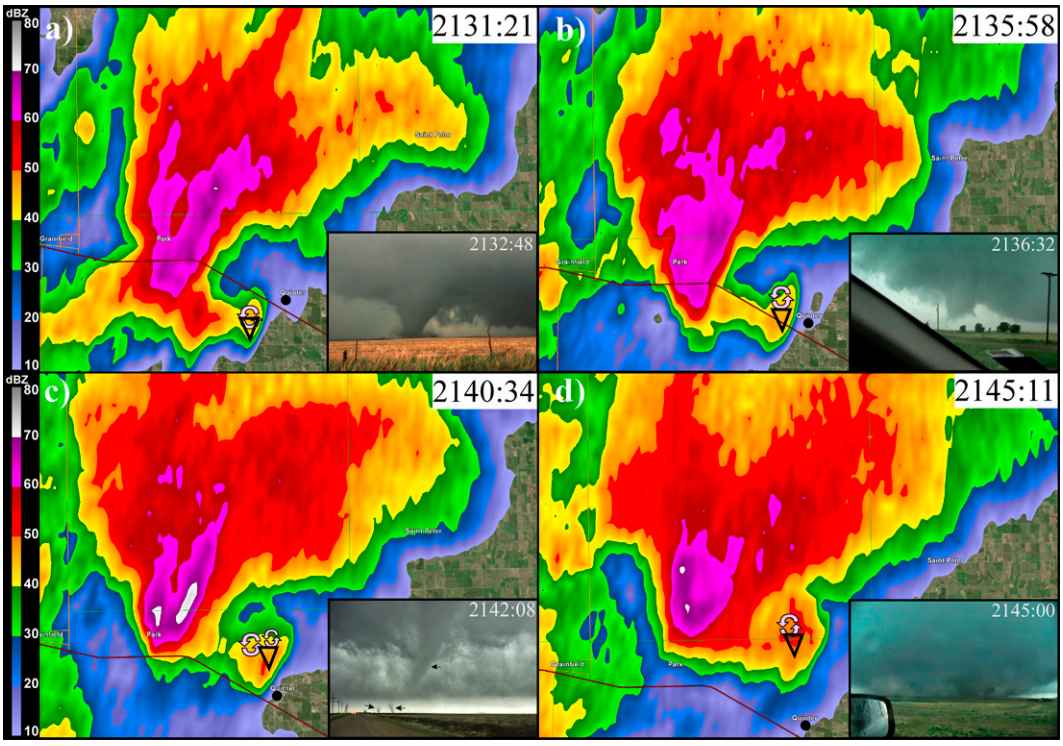

FIG. 3. KGLD 0.5° reflectivity (dBZ) for (a) 2131:21, (b) 2135:58, (c) 2140:34, and (d) 2145:11 UTC. Respective image insets show the mature stage of first tornado in Fig. 2 [in (a); from TWISTEX M2 looking west from ~2.4 km], late stage of same tornado [in (b); from TWISTEX M1 looking west from ~1.5 km], mature stage of second tornado in Fig. 2 [in (c); image courtesy D. Kiesling looking north from ~0.8 km, arrows locate multiple vortices and main funnel in low-contrast lighting], and rapid widening phase of QT coinciding with intense RFIS [in (d); image courtesy C. Collura looking north from ~1.2 km]. Rotation symbols indicate the mesocyclone or submesocyclone centroid. Triangles represent estimated position of respective tornadoes at radar scan time. Quinter location represented with black dot. Storm tilt to the north-northeast with height is responsible for surface tornado locations appearing slightly south of their expected hook echo tip-relative position at ~130 km east-southeast of the radar.

RFIS is under way. The authors have observed a pattern where the hook echo tip and associated circulation accelerates toward a downshear location along the forward-flank reflectivity gradient (FFRG). The "downshear" aspect distinguishes this storm-relative hook echo evolution from a more typical occlusion cycle where the tornado and parent circulation weaken as it gradually moves left of the storm updraft track and transitions to a rearward storm-relative position well removed from the primary storm updraft and deeper into the supercell cold pool (e.g., Burgess et al. 1982; Adlerman et al. 1999; DB02; Beck et al. 2006; Lemon and Umscheid 2008; Tanamachi et al. 2012; French and Kingfield 2019). Coincident with this QS hook echo tip evolution was the presence of a major RFIS, and with it, a significant change in tornado track.

The rapidity with which the QS hook echo tip moves toward the FFRG, concurrent with a powerful RFIS and accompanied by a leftward QT turn, can be seen between the 2040:34 and 2145:11 UTC in Figs. 3c,d. Calculation of the FFRG-relative hook echo tip motion using the 0.5° radial velocity couplet yielded an 8.2 m s^{-1} FFRG-relative speed. Another estimate of the FFRG-relative hook echo tip speed of about 9 m s^{-1} was found using a hook echo tip edge reflectivity-prescribed approach. Reflectivity changes in the hook echo tip due to additional scatterers make this estimate less accurate. Placed in a practical construct, the supercell weak echo region of Fig. 3c closes in the time of just one volume scan as the northern part of the hook echo tip and accompanying circulation approaches the FFRG. The QT speed based on TVS positions post RFIS impact was nearly 20% faster than the mean speed of the two preceding tornadoes. Increased RFIS outflow momentum appeared to influence storm-relative hook echo tip and QT motion consistent with DB02.

At closer range, sensing of a large RFIS in the radar radial velocity field is often possible, but for the QS, the RFIS did not attain a depth sufficient for adequate sampling. For the KGDL 0.5° radial velocity imagery in Fig. 4, the beam height ARL is ~2100 m proximate to the RF. At 2140:52 UTC the QS mesocyclone is poorly organized with two rotation centers,[4] but concurrent with the development of a major RFIS,

[4] The northeastern circulation is associated with the ongoing tornado depicted in Fig. 3c and Fig. 4a and represented by the second track in Fig. 2. This circulation was also evident in the prior two radial velocity scans from KGLD.

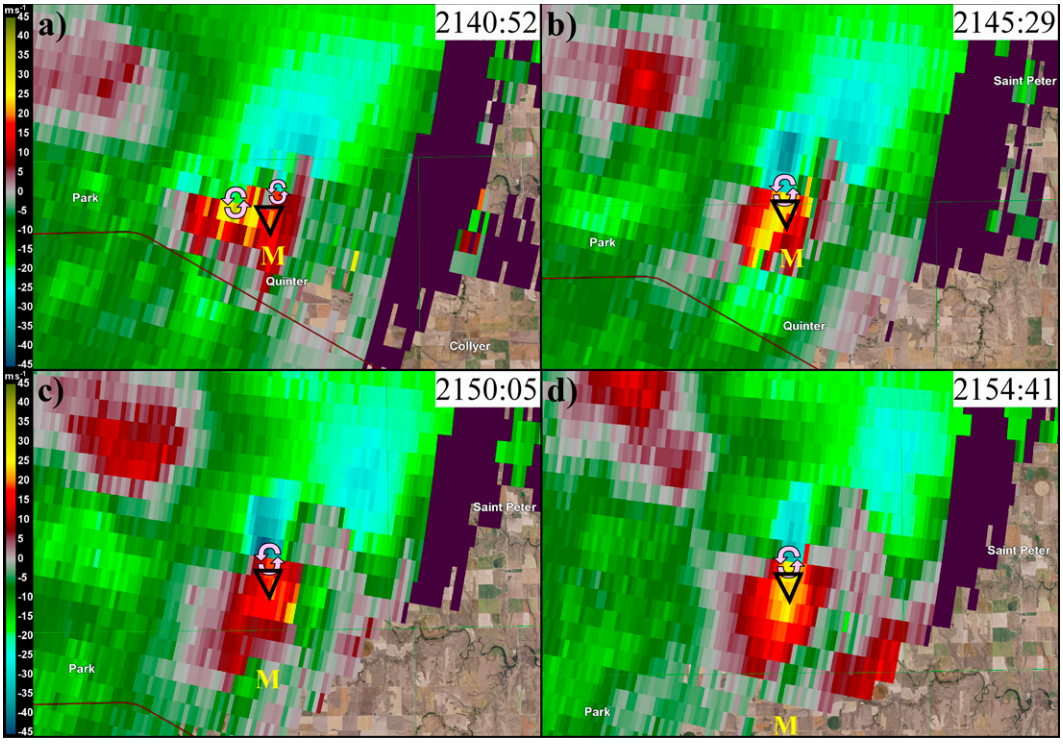

FIG. 4. KGLD 0.5° radial velocity (m s^{-1}) for (a) 2140:52, (b) 2145:29, (c) 2150:05, and (d) 2154:41 UTC. Rotation symbols indicate mesocyclone or submesocyclone centroid and triangles represent estimated position of respective tornadoes at radar scan time. The yellow M is the position of mesonet vehicle M1. Maroon line is Interstate Highway 70. Note that the northeastern rotation center in (a) is associated with the parent circulation of the second tornado shown in Fig. 2 and depicted in Fig. 3c.

by 2145:29 UTC the mesocyclone rapidly gained symmetry. This evolution is similar to that documented by Magsig and Austin (2014) for the 31 May 2013 El Reno tornado event. Even though at 2145:29 UTC the RFIS winds near the surface were high as detailed below, the symmetric radial velocity dipole does not provide a clear signal that a major surge is in progress. Moving forward through two additional volume scans, the inbound–outbound signature maintains rough symmetry and no RFIS signal is evident.

TWISTEX mobile mesonet observations support radar reflectivity inferences of a strong RFIS evolving within the broader RF outflow. M1, the most northward station (Fig. 4) and nearest to the QT, sampled the evolving RF up to the point where northward pursuit was no longer possible. RFGF and RFISB transect times are indicated in the kinematic and thermodynamic time series in Fig. 5. While the kinematic gradient associated with the RFGF transect is evident with veering winds and a speed increase of about 14 m s^{-1} just prior to 2134 UTC, the thermodynamic gradient is particularly marked. The equivalent potential temperature (θ_e) initial drop is steep, losing over 5 K in less than a minute. Both the virtual potential temperature (θ_v) and θ_e drop markedly over about an 8-min period with deficits from storm inflow values reaching 4.7 and 17 K, respectively, as M1 moves farther into the RF outflow. The RF outflow of developing or ongoing significant tornadoes is usually much less negatively buoyant (smaller θ_v deficits) and has smaller θ_e deficits, (Markowski et al. 2002; Grzych et al. 2007; Hirth et al. 2008; Lee et al. 2011, 2012; Weiss et al. 2015) except nearer to the tornado decay stage (e.g., Hirth et al. 2008; Lee et al. 2012; Richardson et al. 2012). What next transpired, both kinematically and thermodynamically, was quite remarkable. As the major RFIS moves over M1, the wind direction backed while speeds ramped up dramatically with a 37 m s^{-1} increase and peak instantaneous 48 m s^{-1} gust. Similarly striking, θ_e jumped 12 K in just 3 min while the θ_v deficit decreased to 1.4 K representing a large reduction in negative buoyancy. This warming continued such that by 7 min post-RFISB passage, θ_v increased to about the storm-inflow value, bearing in mind, M1 is still deep in the RF outflow. Due to the RFIS the tornado-proximate air flanking the low-level rotation centroid on at least the southern and eastern sides possessed thermodynamics and kinematics (e.g., Lee et al. 2012; Kosiba et al. 2013) favorable for significant tornadoes.

b. 31 May 2013 El Reno, Oklahoma, tornado

1) EVENT OVERVIEW

The El Reno tornado (ERT, Fig. 6) was the second in a series of nine tornadoes that occurred in the El Reno–Oklahoma City region of central Oklahoma that were associated with the first

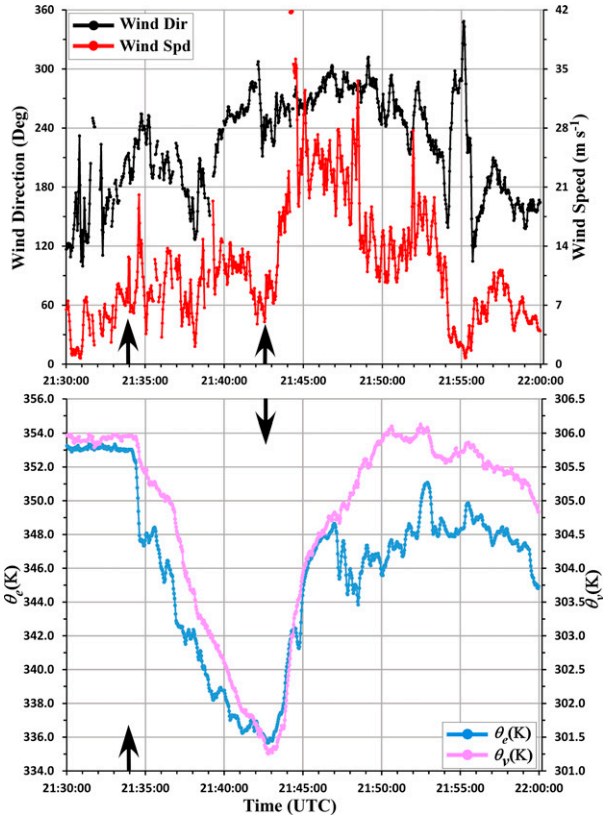

FIG. 5. (top) M1 mesonet station time series of wind direction (°) and speed (m s^{-1}), and (bottom) for θ_e (K) and θ_v (K). Times series are of 6-s averages for all quantities. Arrows represent the leading edges of the RFGF and major RFIS boundary, respectively.

two of a set of three supercells moving quasi-parallel to Interstate 40 (*Storm Data*, NCDC 2013; Bluestein et al. 2015). The ERT developed ~13 km west-southwest of El Reno (Fig. 7) at 2303 UTC and was the most intense and long-lived of the family of tornadoes spawned by the lead supercell, referred to as the El Reno supercell (ERS). Although the ERT had a notable duration of 41 min and pathlength of 26 km, it was historic in terms of its record width (4.2 km), translation speed of subvortices (79 m s^{-1} Wurman et al. 2014; 77 m s^{-1} Wakimoto et al. 2016; 78 m s^{-1} Bluestein et al. 2018), and peak wind speeds of at least 135 m s^{-1}, comparable to some of the fastest Doppler measurements of tornadic winds (Snyder and Bluestein 2014; Wurman et al. 2014; Bluestein et al. 2015, 2018). The ERT caused 8 fatalities including three colleagues of the authors with extensive field experience. A major tornado track change, the subject of this paper, played a large role in the fatalities and near fatalities (Hargrove 2018) as did evolving subvortex structure (Wurman et al. 2014; Wakimoto et al. 2016).

The ERT major leftward heading change near U.S. Highway 81 (U.S.-81) is a key focus area of this analysis as it was contemporaneous with a very high-end RFIS. The intensity of this RFIS was extraordinary as documented by Magsig and Austin (2014) who describe it as "massive" and report radar-indicated RF outflow winds topping 63 m s^{-1} near the onset

FIG. 6. ERT viewed from 6 km to the southeast at 2325:49 UTC. At this time the tornado was moving to the northeast after having made a marked left turn. Rear-flank downdraft (and outflow beneath it) is associated with the lighter slot in the storm base bounding the west and south side of the ERS mesocyclone. A prominent secondary vortex of the ERT can be seen with front-lit condensation extending to the surface. This was the same subvortex cited in the text with having the highest Doppler-indicated translational speed yet recorded (A. Seimon videographic comparison with mobile radar data; Pecos Hank 2020). Photograph courtesy of J. Brindley Ubl.

of the ERT left turn. Similarly, Bluestein et al. (2015) describe the RF winds as "extremely intense" while presenting RaX-Pol observations of RF winds of 55–60 m s^{-1} just prior to the left turn.[5] They note the extreme magnitude of the RF outflow might have been aided by a superposition of outflow on a larger-diameter vortex. *Storm Data* (NCDC 2013) reported a damage swath much larger than the tornado width with non-tornadic downdraft wind damage (i.e., from RF outflow) extending at least a mile south of the tornado.

2) TORNADO TRACK

In the NWS tornado track (Fig. 7) the ERT executed three very large heading changes with the second of these the primary focus of this analysis. Starting at 2303 UTC the first segment of the ERT track had a southeastward heading (146°) for the first several kilometers. This direction was somewhat unusual for a storm at that time having an eastward heading based on differential radar reflectivity factor (Z_{DR}) column tracking (French and Kingfield 2019). However, during this period the hook echo was developing to the southeast. Over the second track segment the tornado moved with a mean easterly heading (92°) to the point it crossed U.S.-81 at 2319 UTC. This heading was consistent with that of its parent supercell. After crossing U.S.-81 the tornado turned markedly to the left about 55° and assumed a generally northeasterly heading (37°) between U.S.-81 and Interstate 40 (I-40). Of importance, this major heading change occurred concurrent with the "massive" RFIS that Magsig and Austin

[5] The heighted danger of the ERT evolution is captured from a field observer's perspective in the following videos: https://www.youtube.com/watch?v=TBjr-nvA2Jg&t=1121s (NWS Norman, OK), https://www.youtube.com/watch?v=bJOjjzHUwsk (S. Talbot).

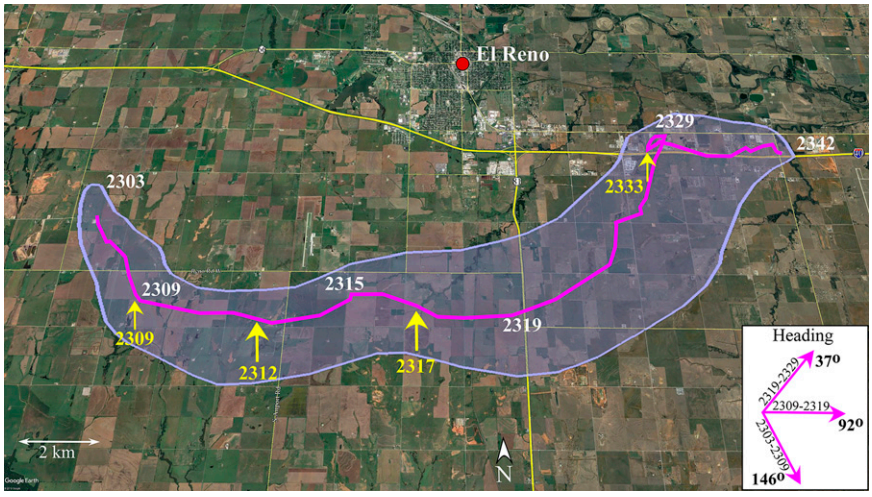

FIG. 7. ERT damage path from the NWS Forecast Office in Norman, OK, is outlined in light purple. Damage path and width is derived from the official damage survey with the track width determination aided by radar data from the University of Oklahoma RaXPol. Both RaXPol and WSR-88D data were used in the creation of the center vortex track and chronology shown with the magenta line (NOAA 2014). Times are in UTC. Yellow arrows and times show the approximate radar-estimated track-relative location and time of RFIS impacts with the ERT featured in section 3b(3). Larger arrows correspond to major surges analyzed in detail. The inset shows mean ERT headings for the first three track segments identified in the text along with times on those headings. The bold quasi west–east (north–south) yellow line is I-40 (U.S.-81).

(2014) referred to. Noteworthy is that this large left turn occurred at a time the ERS heading was about 95°. As the ERT neared and crossed north of I-40 it slowed markedly with the tornado core executing a tight loop. Exiting the loop at about 2335 UTC, the tornado once again assumed a nearly easterly heading consistent with the ERS motion.

3) HOOK ECHO AND RF EVOLUTION WITH ERT MOTION CHANGES

The radar-indicated hook echo and RF outflow evolutions were analyzed for the ERS with special emphasis given to the period leading up to, during, and just following the second major ERT track change (Figs. 8, 9, 10). For perspective, from the beginning to the end of the second track segment (2309–2319 UTC) shown in Fig. 7 KTLX and MPAR distances to the ERT ranged from 72 to 61 km and from 59 to 49 km, respectively. By approximately the start of the long-duration ERT, KTLX showed a well-defined radar reflectivity hook and LLM (Figs. 8a, 9a). Prior to the development of the high-end RFIS temporally associated with the ERT U.S.-81 turn, a RFIS rapidly developed between about 2306 and 2310 UTC. The leading edge of this surge is evident in KTLX imagery with a sharpening inbound radial velocity gradient south of the tornado (Fig. 9b). MPAR imagery supports this conclusion with the timing of surge intensification around 2309 UTC (not shown). Notably, the ERT makes a sharp direction change to an easterly heading (Fig. 7) at about the time of surge strengthening while also displaying a marked increase in speed (Fig. 11).

Over the following several minutes the next RFIS quickly developed and grew markedly in size and intensity as depicted in KTLX and MPAR imagery. The first indication of this surge on MPAR was at 2311:05 UTC about 3 km northwest of the ERT (Fig. 10). Unlike the prior RFIS that was largely positioned south of the tornado, in this much stronger and larger surge, MPAR imagery depicted flow with a strong westerly component developing to the west of the tornado. While the KTLX imagery (Figs. 9c,d) also captures this evolution, the utility of the high-temporal resolution of MPAR is readily apparent. The approximate impact time of this surge on the ERT was estimated from MPAR to occur just after ~2312:16 UTC, a period corresponding to a sharp increase in tornado speed and preceding a local temporal maximum in tornado speed (22 m s^{-1}, Fig. 11). Following about a 2-min period of reduced tornado speed that corresponds with a short duration northward turn of the ERT seen in Fig. 7 that is captured with superior fidelity in the combined damage survey and radar analysis of Wakimoto et al. (2016, see their Fig. 8), the ERT accelerated eastward again, especially after 2317:00 UTC (Fig. 11). This period corresponds with either a sharp intensity ramp within the prevailing RFIS or a new surge (Fig. 10). Temporal radar data limitations make a confident designation difficult in this rapidly evolving flow field. Being immersed to a substantial degree in a flow field with strong westerly momentum, the ERT reached a peak speed of 24 m s^{-1} as it approached U.S.-81 representing a 91% increase in speed compared with the average tornado speed prior to the major RFIS. This peak speed is in close agreement with the 25 m s^{-1} speed ascertained near this location by Doppler on Wheels mobile radar (Wurman et al. 2014). The tornado motion for this

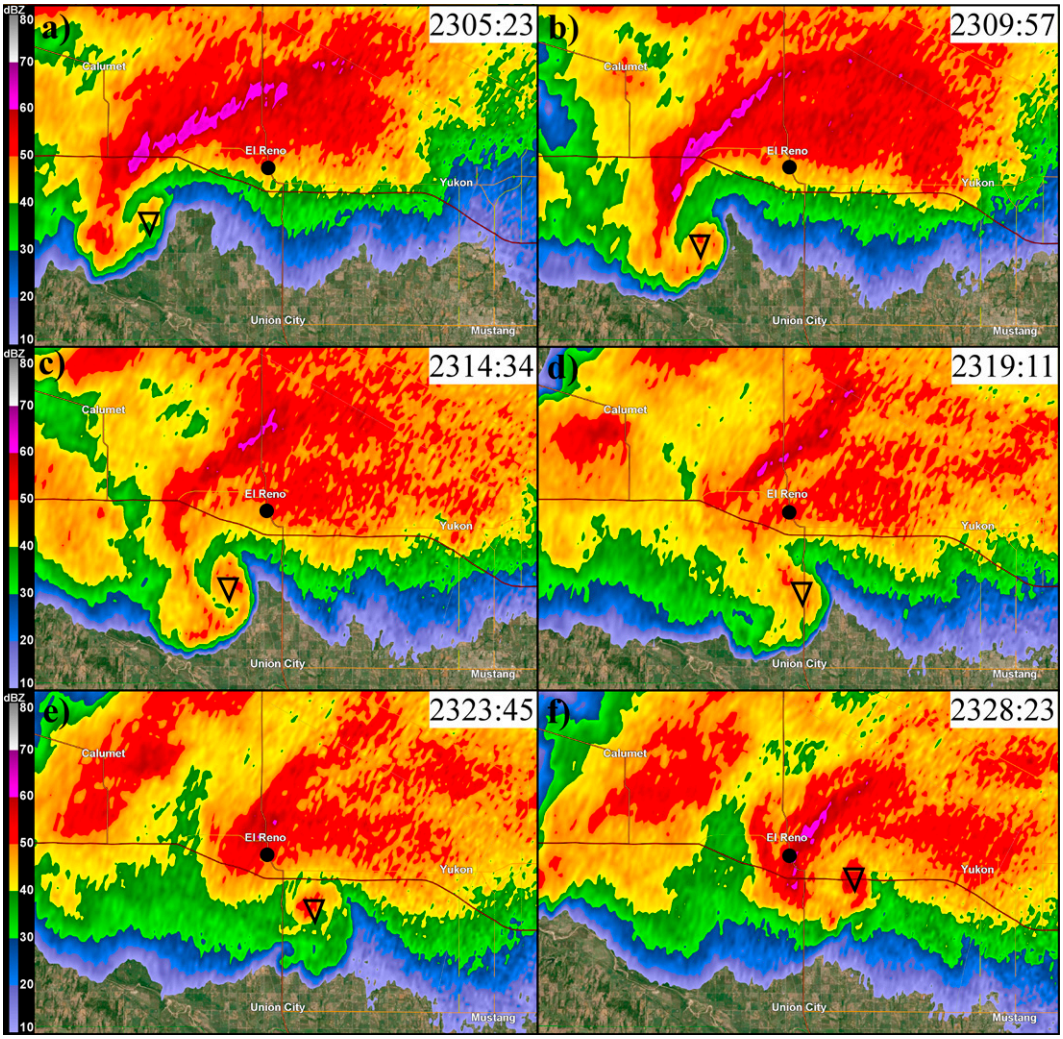

FIG. 8. KTLX 0.5° reflectivity (dBZ) for (a) 2305:23, (b) 2309:57, (c) 2314:34, (d) 2319:11, (e) 2323:45, and (f) 2328:23 UTC. Triangles represent estimated tornado position at radar scan time. KTLX is about 65 km east-southeast of El Reno (black dot).

segment appeared consistent with a mismatch between the very strong RF outflow and storm inflow consistent with DB02 and found in subsequent cases (e.g., Marquis et al. 2012; French et al. 2014; Houser et al. 2015). Note the associated hook echo neck eastward reorientation under way in Fig. 8d that is in apparent response to the alteration in proximate momentum balance. As the ERT approached and crossed U.S.-81, RF flow within the surge became extraordinarily strong with peak radial velocities from MPAR of at least 63 m s^{-1} (Fig. 10d) at ~610 m ARL. These speeds are consistent with peak radial velocities near this time from nearby KCRI-88D radar reported on by Magsig and Austin (2014). KTLX maximum 0.5° RF radial winds near this time were at least 60 m s^{-1} (Fig. 9d). Actual peak speeds were likely stronger since only the radial component was sensed. For a visual perspective of what near-ground conditions were like inside this powerful RFIS, the reader is directed to team videos in the TED (http://el-reno-survey.net/ted) that were positioned west and south of the tornado (especially the Casey and Gwyn teams) near and within a few minutes after the ERT crosses U.S.-81 at ~2319 UTC.

The major ERT leftward turn occurred just after it passed U.S.-81 and at a time when the core of the RFIS was evolving such that the westerly momentum weakened to the west of the tornado. This evolution is readily apparent from 2319:28 to 2324:03 UTC on KTLX (Figs. 9d,e) as the tornado-relative geographical centroid of the surge rotates from west-southwest of the ERT toward a southerly position. In higher-temporal resolution, MPAR showed the beginning of the trend (Fig. 10) between 2317:00 and 2320:33 UTC. As the core of the RFIS translates south of the tornado, expected divergence within the surge would associate with a southerly momentum component in the flow field bounding the tornado to its south. Coupled with the weakened, but still substantial, westerly momentum component within the surge, the tornado and LLM are impacted by the surge's southwesterly momentum. Associated with this tornado-relative change in bounding

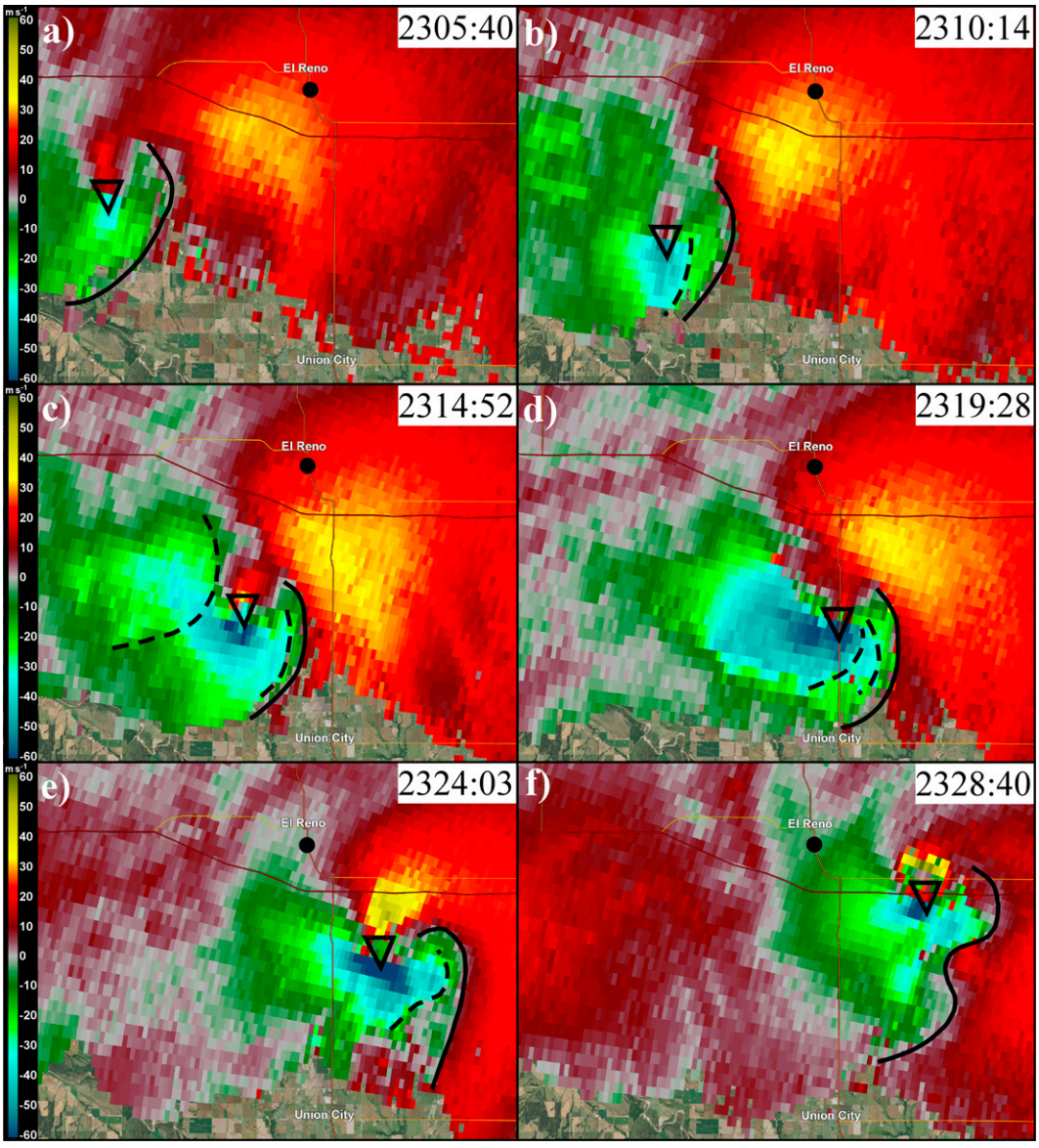

FIG. 9. KTLX 0.5° radial velocity (m s^{-1}) for (a) 2305:40, (b) 2310:14, (c) 2314:52, (d) 2319:28, (e) 2324:03, and (f) 2328:40 UTC. Triangles represent estimated position of ERT at radar scan time. Solid lines depict the RFGF and dashed lines the RFISBs. El Reno is represented with a black dot.

momentum directionality, the hook echo tip moves rapidly northeastward toward the FFRG at a storm-relative downshear location (Figs. 8e,f). Using a similar technique as employed in the QS analysis, the LLM associated with the hook echo tip had a FFRG-relative speed of 9.2 m s^{-1}. At this speed, the supercell weak echo region at 2319:11 UTC (Fig. 8d) closes in just about 1.5 traditional volume scan periods. Note that several minutes after the tornado center crossed I-40 (Fig. 7), there is some indication from KTLX and stronger evidence from KCRI-88D imagery presented by Magsig and Austin (2014) that a RFIS was temporally associated with the ERT accelerating to the east (Fig. 11).

Noteworthy in this event was the duration of the ERT after the large heading change at ~2319 UTC. Lasting 23 min beyond this turn, from longevity and storm updraft relative track perspectives, the ERT stands in contrast to a typical occlusion cycle that places the tornado deeper into the supercell cold pool and displaced rearward from the storm updraft. The storm-relative motion of the ERT after its U.S.-81 turn (left and forward) may have delayed the circulation from becoming immersed in more negatively buoyant air farther rearward in the storm and kept it more closely aligned with the storm updraft. Notably, tornado intensity appears to have peaked approximately 6–7 min following its

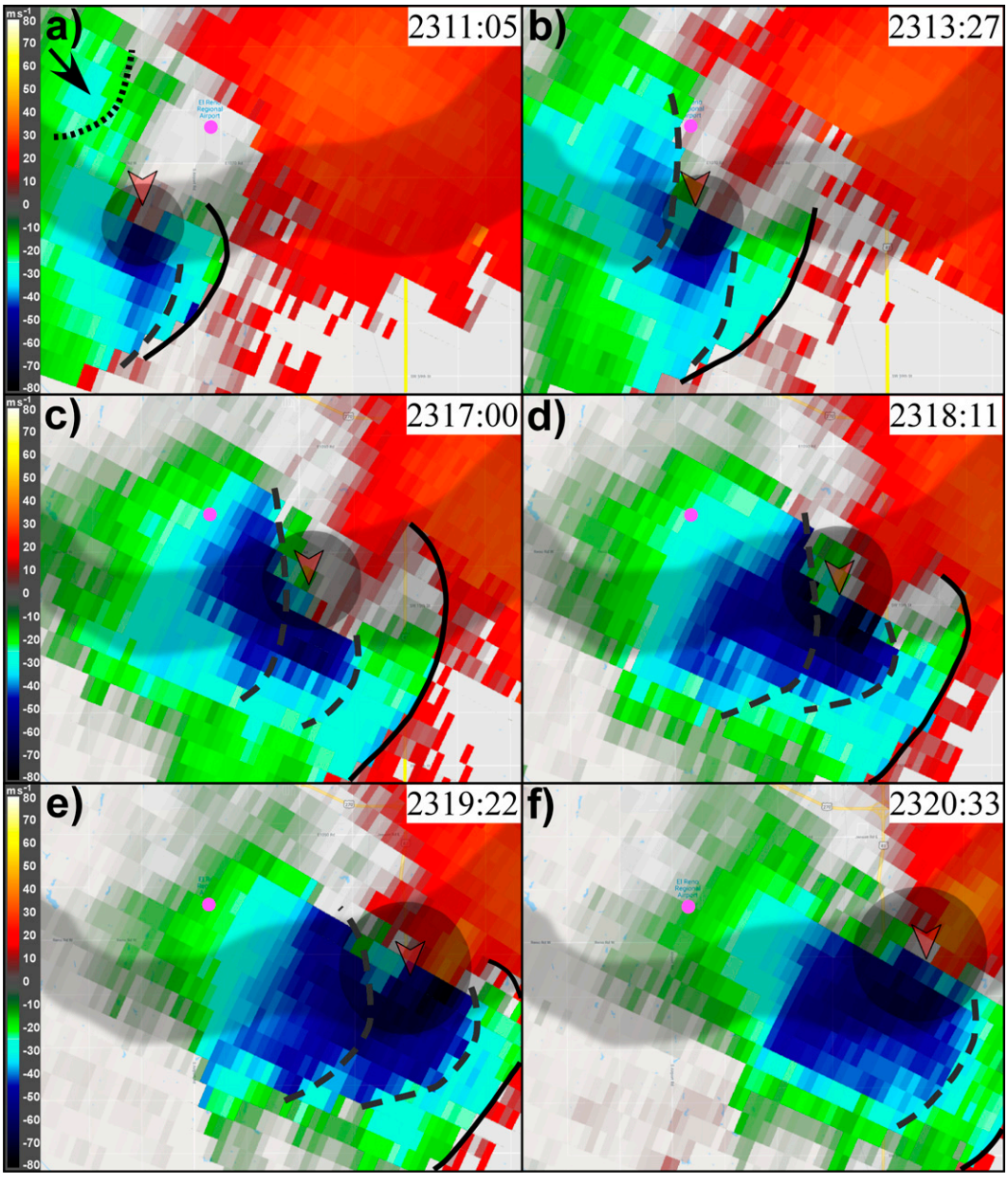

FIG. 10. MPAR 0.5° radial velocity (m s^{-1}) at (a) 2311:05, (b) 2313:27, (c) 2317:00, (d) 2318:11, (e) 2319:22, and (f) 2320:33 UTC. The arrow tip locates the radar-indicated vortex center, and the shaded track is the NWS official damage track. The darker-shaded circle represents an approximation of a tornado with a diameter consistent with the damage path. Solid lines depict the RFGF and dashed lines the RFISBs. The arrow and dotted line in (a) show the location and approximate leading edge of the eventual major RFIS where first indicated. MPAR is about 56 km east-southeast of the El Reno airport (magenta dot). MPAR imagery display is that used in TED.

marked northeastward turn near U.S.-81 (Snyder and Bluestein 2014; Wurman et al. 2014, Wakimoto et al. 2016).

c. 11 July 2017 Hillsboro, North Dakota, tornado

1) EVENT OVERVIEW

On the evening of 11 July 2017 at least seven supercell thunderstorms traversed eastern North Dakota and into northwestern Minnesota spawning 11 tornadoes (*Storm Data*, NCDC 2017). The southernmost supercell of this group designated the Hillsboro supercell (HS) was the largest and longest-lived, and responsible for four tornadoes of which three were the most intense of the event. The large second tornado of this series designated the Hillsboro tornado (HT) developed at 2358 UTC 16 km west-northwest of Buxton, North Dakota (Fig. 12). The HT lasted ~51 min, had peak winds

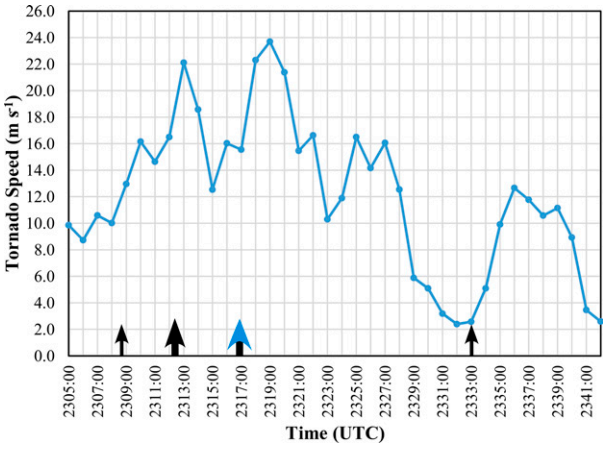

FIG. 11. ERT speed (m s^{-1}) time series. Arrows refer to estimated onset times of RFIS impacts on the ERT. Arrow width reflects relative strength of the RFIS. The blue arrowhead represents either a sharp intensity ramp in the prevailing surge or a strong new surge.

estimated at the upper-end of the EF2 range (60 m s^{-1}), and exhibited a maximum width of 1100 m. The lack of visibility in this event elevated the risk as the HT was largely obscured by precipitation outside of a period of early intensification (Fig. 13). The next tornado in the officially reported HS family, designated the Halstad, Minnesota, tornado (HMT), also of high-end EF2 intensity and with a peak width of 550 m, formed at 0048 UTC 12 km west-northwest of Halstad. The HMT officially formed just before the HT dissipated and lasted 23 min. In contrast to the official reporting, ample radar evidence suggests that there was no well-defined conclusion of the HT and beginning of the HMT. We consider this a 73-min continuous tornado (2358–0111 UTC) and will address this issue in sections 3c(2) and 3c(3). A notable statistic for the HS was that between 2325 and 0206 UTC a tornado was ongoing for nearly 2 h.

A key aspect of the Hillsboro storm that applies directly to the subject of this paper involves two powerful RFISs, the first of which occurred about 45 min into the HT. The Grand Forks NWS event overview mentioned "extreme downburst winds of from 80 to 100 mph (36–45 m s^{-1}) raked across the community of Hillsboro" (weather.gov/fgf/2017_July11Severe). The emphasis of the following analysis is on the temporal association between these RFISs and substantial tornado motion changes.

2) TORNADO TRACK

The HT tornado track and key times are presented in Fig. 12. The track and chronology were largely developed through analysis of KMVX data. NWS damage track information (https://www.weather.gov/fgf/2017_July11Severe) was primarily used early (2358–0009 UTC) and at the very end of the tornado, and also in consistency checks with radar-derived tornado positions. KMVX was fortuitously close to the HT lending confidence to

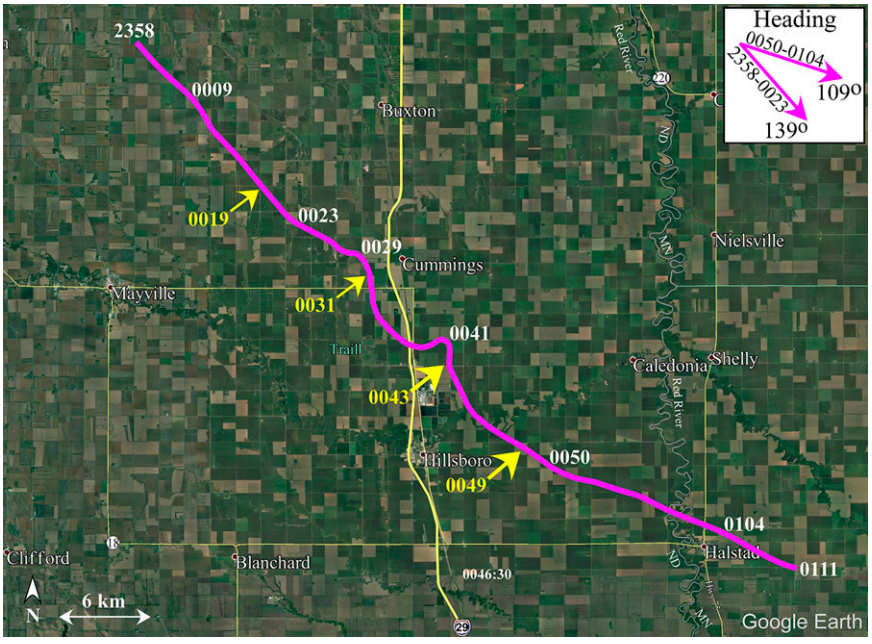

FIG. 12. Annotated tornado track for the HT. Times (UTC) internal to the tornado start and end points are radar-derived. Yellow arrows and times show the approximate radar-estimated track-relative location and time of RFIS impacts with the HT featured in section 3c(3). Larger arrows correspond to major surges analyzed in detail. The inset shows HT headings for indicated representative periods prior to approaching I-29 and after completion of a longer-duration leftward turn (~0050 UTC). The bold light yellow line is I-29.

FIG. 13. Fully condensed secondary vortex in the early intensification stage of the HT at 0010:27 UTC from the lead author's location approximately 2.5 km to the east.

the radar analysis while providing time/position information for the tornado at ~120-s intervals that offered additional track detail that was not available in the damage survey. Nearly 75% of the track was within 35 km (2358–0052 UTC) of KMVX. Specifically, inside of about 35 km from KMVX and beyond about the first 10 min of the HT (where the damage track was favored over inadequate radar evidence of tornado position), tornado locations were readily identified in lowest-level radial velocity shear signatures that were often accompanied by a TDS. Beyond 35 km (after 0052 UTC) as the tornadic region transitioned to a multiple vortex mesocyclone (MVMC; Wurman and Kosiba 2013; Wurman et al. 2014), other products like normalized rotation (Lemon and Umscheid 2008; Nielson and Schumacher 2020) and spectrum width patterns were additionally employed in estimating the approximate tornadic MVMC centroid. The tornado track in Fig. 12 beyond 0052 UTC reflects the estimated MVMC centroid. We will further address radar aspects of this MVMC transition in section 3c(3).

Of prominent interest in this study, the HT displayed a longer-duration tornado track change of 30° subsequent with the development and merger of two major RFISs. The HT tornado had a consistent heading of ~139° over its first 25 min, and similar heading when averaged out over its path up to Interstate 29 (I-29); however, as it grew close to, and passed I-29, the tornado track changed markedly multiple times. This period of large track changes was temporally associated with RFISs (Fig. 12) to be analyzed in section 3c(3). During the time the HT was near I-29, two distinct heading-change cycles are evident, that latter of which featured a cusp-like pattern (e.g., Wakimoto et al. 2016) of abrupt direction change centered on 0041 UTC. In contrast to these shorter-duration track-change cycles, a leftward heading change regime is apparent between about 0043 and 0050 UTC that leads to a longer-duration period where the mean tornado heading is 109°, a 30° change from the HT mean direction prior to crossing I-29. The next tornado for the HS began 31 min later about 5 km north of Borup, Minnesota. This high-end EF2 tornado maintained a heading of ~130° over a large majority of its 24-min existence. Notably, this tornado's heading was much closer to that of the HT prior to the longer-duration leftward turn.

3) HOOK ECHO AND RF EVOLUTION WITH HT MOTION CHANGES

The HS hook echo region was analyzed between 0011 and 0108 UTC representing a period that captured the RF evolution from the early intensification stage of the HT through the MVMC phase of the event (Figs. 14 and 15). Particular attention was focused on the two RFISs associated with the longer-duration change in tornado track. Over the first ~70% of the analysis period (0011–0050 UTC) the tornado was located between 9 and 31 km from KMVX with a lowest tilt center beam scan height (ARL) residing between approximately 100 and 325 m ARL. By the end of the analysis period (0108 UTC) the HT was 48 km from KMVX with lowest tilt scanning at ~550 m ARL. While two official tornadoes were recorded over this period, from a radar perspective, the parent LLM was common to both without separate occlusion cycles. A TDS and accompanying shear signature existed along a path connecting the official HT and HMT tracks (not shown). Additionally, a reflectivity debris ball evident in Fig. 14e and collocated with a TDS was tracked from 0046:12 to 0051:59 UTC. Moreover, radial velocity analysis reveals that the long-lived tornadic circulation was a prominent vortex incorporating into the developing MVMC. From an operational continuity perspective, we consider this a long-track (57 km) and duration (73 min) tornado event.

The RF outflow within and near the HS hook echo region markedly expanded over the course of the HT, especially during the period from the HT early maturation through the MVMC stages. Several RFISs promoted this expansion. Relative to the late panels of Fig. 15, the RF outflow was compact at 0013:07 UTC (Fig. 15a). Near this time the hook echo tip had completely coiled around the low-level circulation (Fig. 14a) as the already-wide tornado with a 1300-m TDS (not shown) strengthened (ΔV_{max} of 84 m s^{-1}). By 0026:39 UTC the RF outflow footprint expanded due in large part to momentum surges (Fig. 15b), one of which that occurred several minutes prior, was associated with a local temporal maximum in tornado speed (Fig. 16). At this time a well-defined weak-echo hole (e.g., Fujita 1981; Wakimoto and Martner 1992; Wurman and Gill 2000; Bluestein et al. 2004, 2007) was present that identifies the HT centroid (Fig. 14b). The leading edge of another RFIS is shown at 0032:59 UTC (Fig. 15c). This surge possessed a peak radial wind speed of 42 m s^{-1} at ~180 m ARL. The rightward turn of the HT around 0031 UTC (Fig. 12) occurred as this surge altered the tornado-proximate local momentum balance. The HT left track turn as it approached and crossed I-29 at ~0035 UTC (Fig. 12) and leftward/rearward storm-relative position change occurred during a marked drop in near-tornado RF outflow in the wake of this surge consistent with DB02. Associated with this surge, a sharp increase in tornado speed to 19 m s^{-1} was followed by a symmetric speed decrease as the momentum from the surge translated well south of the tornado (Fig. 16).

The next two RFISs appear to have a large influence on the HT track, LLM, and hook echo. The leading edge of the first of these large RFISs is shown in Fig. 15d at 0044:40 UTC just after passing through Hillsboro. Peak KMVX 0.5° outbound radial

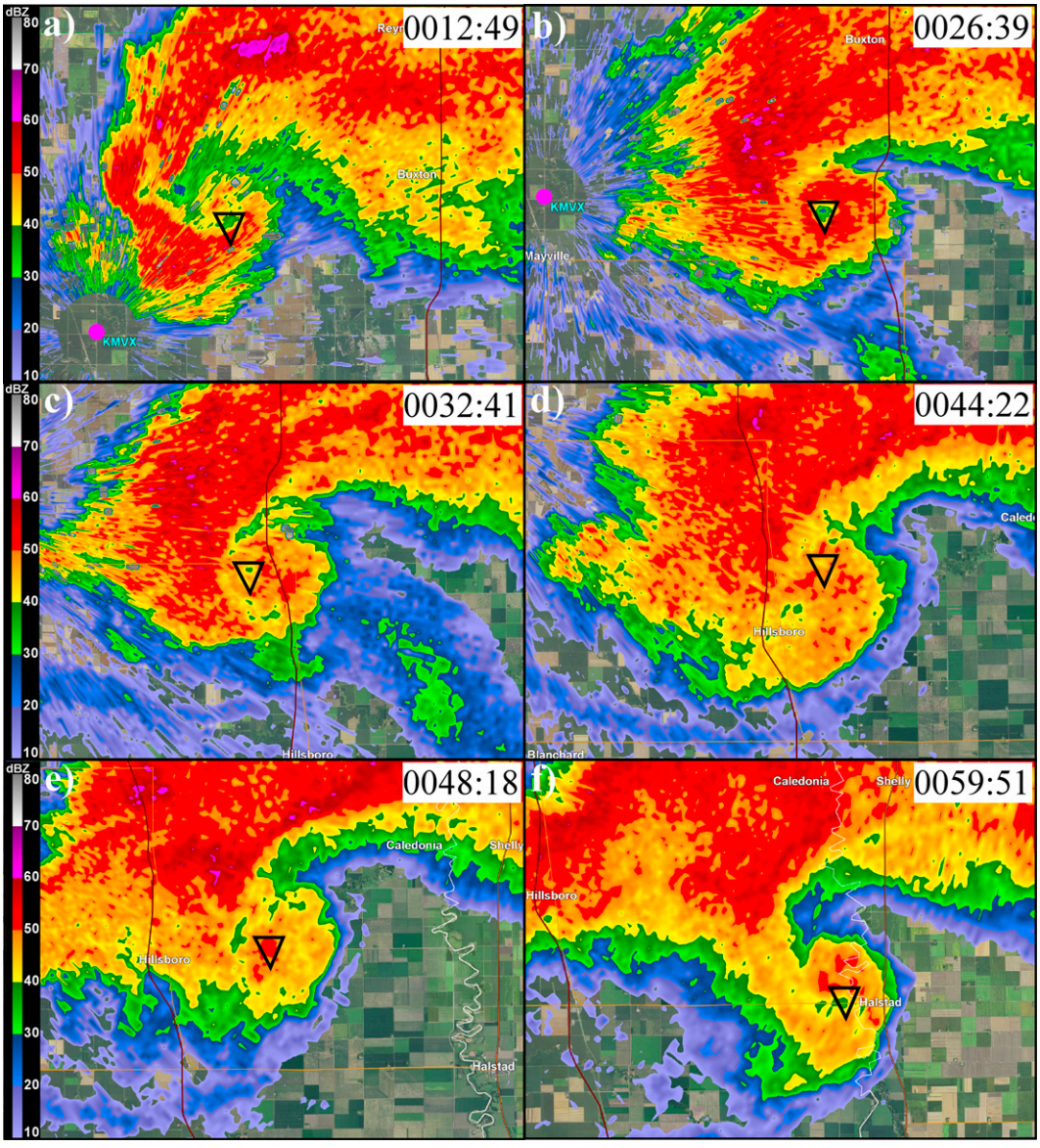

FIG. 14. KMVX 0.5° reflectivity (dBZ) for (a) 0012:49:23, (b) 0026:39, (c) 0032:41, (d) 0044:22, (e) 0048:18, and (f) 0059:51 UTC. Triangles represent estimated tornado position at radar scan time. KMVX location is indicated with a magenta dot.

wind speed within the RFIS at this time was 46 m s^{-1} at ~250 m ARL, positionally and temporally consistent with the aforementioned NWS damage assessment for Hillsboro. The HT right turn after ~0041 UTC (Fig. 12) was associated with this surge as northwesterly tornado-proximate momentum increased markedly. The tornado speed increase beginning near the approximate surge impact time was commensurately large with the speed doubling in just 3.7 min to 21 m s^{-1} (Fig. 16). The first sign of the second of these major surges was at 0044:40 UTC (Fig. 15d), but is far more obvious by 0048:36 UTC (Fig. 15e). Interestingly, this surge looks to have originated in the rear part of the forward-flank outflow region, and subsequently moved south in a storm-relative sense into and through the RF. This behavior is something the authors have seen in their collaborative research with very high-resolution tornadic supercell modeling (Orf et al. 2017; Finley et al. 2018) and in observational cases such as the 17 June 2009 Aurora, Nebraska, tornadic supercell (Lee et al. 2010), and may be similar to surge evolution cited in other observational research (e.g., Houser et al. 2015; Kurdzo et al. 2015). Coinciding with the impact of this second major surge, the HT speed ramps higher to a peak just exceeding 25 m s^{-1} by 0052:17 UTC (Fig. 16). As the two major RFISs merged by ~0050 UTC, an expansive area of very intense RF outflow evolved. Concurrent with the RFIS merger, the HT turned markedly leftward and maintained an approximate 109° mean heading over the majority of its remaining track (Fig. 12). Note that by 0100:09 UTC peak outbound winds of at least 53 m s^{-1} at ~422 m ARL existed within the combined surge (Fig. 15f).

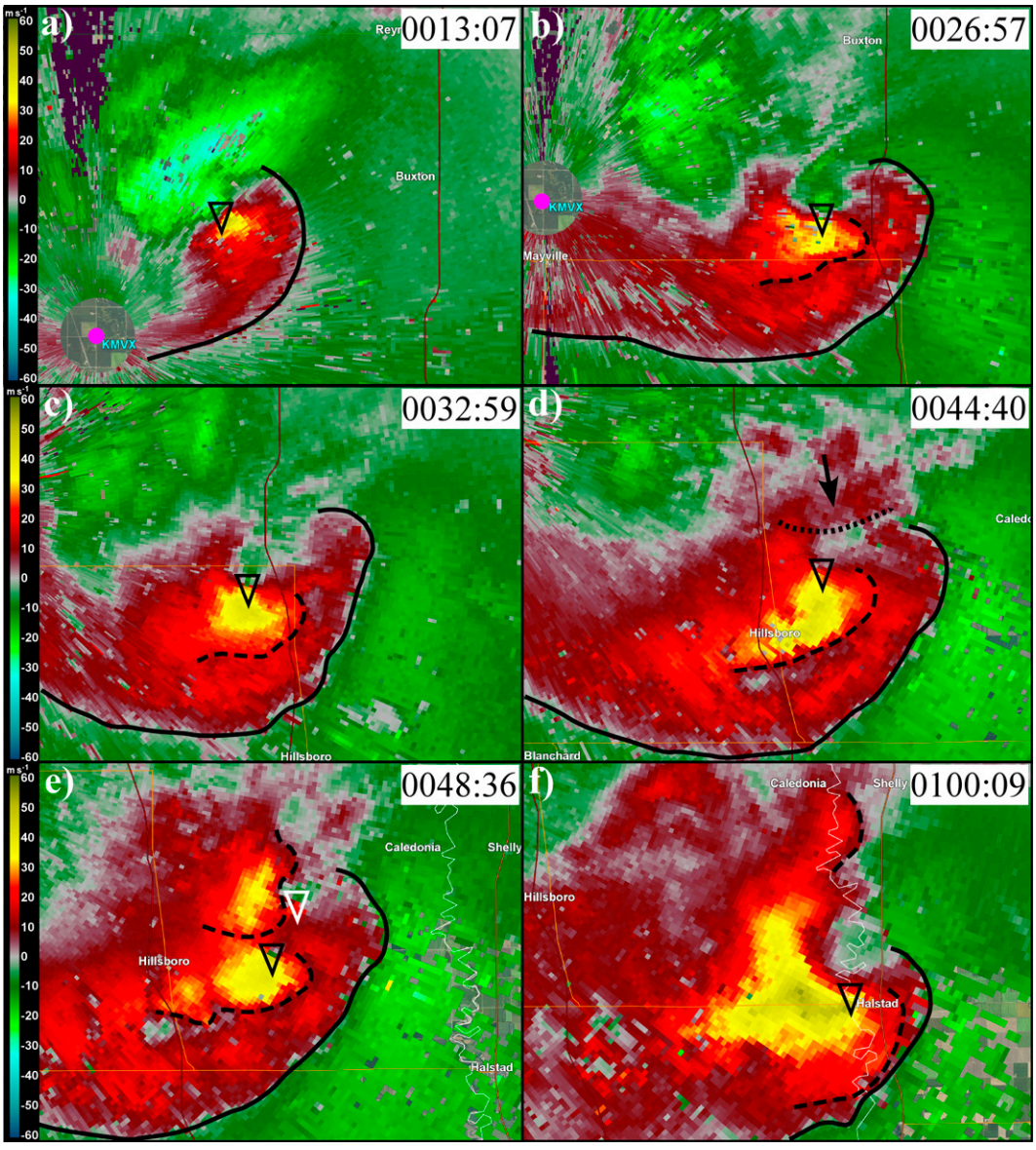

FIG. 15. KMVX 0.5° radial velocity (m s^{-1}) for (a) 0013:07, (b) 0026:57, (c) 0032:59, (d) 0044:40, (e) 0048:36, and (f) 0100:09 UTC. Black triangles represent estimated tornado position at radar scan time. Dark solid lines depict the RFGF and dashed lines the most prominent RFISBs. The arrow and dotted line in (d) show the location and approximate leading edge of the eventual second major RFIS where first indicated. The white triangle in (e) designates the location of a secondary vortex. KMVX location is designated with a magenta dot.

A temporal association exists between the interactions of these major surges with the LLM as the latter transitions to a MVMC structure. A secondary vortex early in this MVMC transition can be seen north-northeast of the primary tornado at 0048:18 UTC in Fig. 15e and its condensation cone was visually observed moving south (consistent with KMVX tracking) by the lead author from a position about 7 km to the east-northeast (Fig. 17). This northern vortex was followed for three consecutive scans in the 0.5° radial velocity, including some ρ_{hv} minima support, as its course took on a cyclonic path with respect to the LLM centroid. The primary tornado also took a cyclonic turn under the influence of the altered LLM structure just prior to being incorporated into the larger diameter tornadic MVMC. This influence may also have briefly contributed to the tornado speed within about 2 min or so of its peak (0052:17 UTC).

Concurrent with the development of a large region of very-strong RF outflow resulting from the intense merging RFISs, the LLM heading turns left between about 0043–0050 UTC to an east-southeasterly direction (Fig. 12). The major increase in RF outflow momentum west and southwest of the tornadic region can be readily seen in Figs. 15d–f. Contemporaneous with

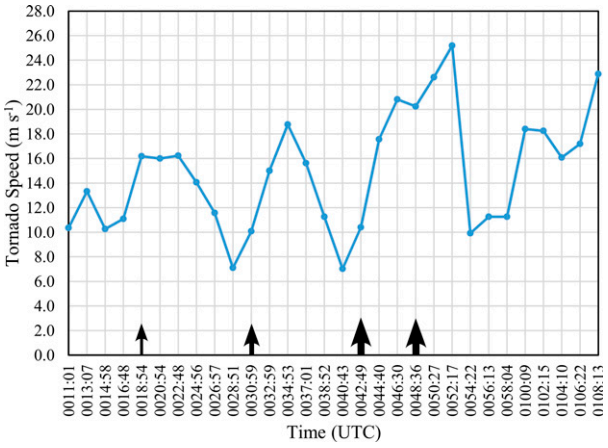

FIG. 16. HT speed (m s^{-1}) time series. Arrows refer to estimated onset times of RFIS impacts on the HT. Arrow width reflects relative strength of the RFIS.

FIG. 17. Condensation cone of the northernmost vortex (see Fig. 15e) of the developing MVMC in the HS at 0049:39 UTC from a vantage point 7 km to the east-northeast.

this LLM track change, the hook-echo tip extends away from the HS reflectivity centroid between 0048:18 and 0059:51 UTC (Figs. 14e,f) and turns leftward. HT motion changes are consistent with an altered storm-relative balance between storm outflow and inflow, and conceptually, with a tornado and parent circulation being directly influenced by changes in the broader flow field they are largely embedded in (DB02; Marquis et al. 2012). The HT generally maintained the new course through the end of this event (~21 min).

4. Summary and discussion

This research has featured the potential utility of monitoring the RF region of tornadic supercells for momentum surges, particularly large and intense ones, as their onset and maturation can be temporally related to substantial tornado heading and speed changes. The RFISs featured had peak winds ranging from the 48 m s^{-1} mesonet reading in the Quinter event to the MPAR readings of at least 63 m s^{-1} in the El Reno case. The surge-associated longer-duration tornado heading changes were leftward and ranged from 30° for the HT to 55° for the ERT. An approximate doubling of the tornado speed was observed for the ERT and HT in association with the strongest surges. A storm-relative change in the hook echo orientation accompanied the major surges and provided an indication that a marked leftward heading change for an ongoing tornado was under way. Concurrent with the surge interaction, the hook echo tip and associated low-level mesocyclone turned leftward while also moving in a storm-relative downshear direction.

In all three cases the tornado lasted well beyond (≥21 min) the time of the RFIS-associated left turn with no apparent loss of intensity until well down-track of the turn. This behavior stands in contrast to typical tornado late-stage behavior where the tornado turns left and moves to a storm-relative rearward position while weakening and ultimately dissipating in a maturing mesocyclone occlusion cycle (e.g., Burgess et al. 1982; DB02; French and Kingfield 2019). This typical dissipation scenario usually places the tornado deeper into the supercell cold pool and displaced from the deep storm updraft, representing primary factors associated with observed tornado decay (e.g., DB02; Hirth et al. 2008; Wurman et al. 2010; Marquis et al. 2012; Lee et al. 2012; Richardson et al. 2012). In all three cases the tornado and its parent circulation were displaced forward and leftward in a storm centroid relative perspective. This flow field configuration kept the tornado in a location closer to the deep-storm updraft, and quite likely in a less-inhibitive thermodynamic environment, facets that would be critical to tornado longevity.

Investigating the dynamical relationship between RFISs and tornado motion changes is best suited for a modeling study where pressure perturbation components can be effectively assessed; however, some physical relationships seem apparent. The conceptual model of DB02 appears appropriate for explaining the tornado-motion deviations presented here, in either heading or speed. Rather similar to the Kurdzo et al. (2015) study of the 20 May 2013 Moore, Oklahoma, EF5 tornado event, the major RFISs influenced tornado motion such that a generally favorable storm updraft-relative position was maintained. The association between surge-related momentum changes and tornado speed changes, evident in Kurdzo et al. was especially apparent in the ERT and HT episodes. The local momentum balance bounding the tornado or its parent circulation, especially the directionality evolution of the bounding momentum, is the most apparent explanation for tornado down-track or off-track accelerations in the featured events. Examining the dynamic drivers for *particularly strong and large* RFISs that markedly alter the tornado-proximate outflow-inflow momentum balance would constitute a valuable research endeavor. Moreover, understanding dynamic connections and feedbacks between these surges and the storm mesocyclone may shed further light on longer-duration tornado deviations similar to the postulation of Magsig and Austin (2014).

At an elemental level, an emerging large and intense radar-indicated RFIS that will impact a tornado elevates *the potential* for a tornado heading and/or speed change while concurrently lowering confidence in an existing tornado warning polygon. Knowledge of this association has utility in providing trend support for observer and/or radar indications of a tornado motion change, and in raising awareness of an enhanced potential for a tornado motion change when a TVS is not being adequately

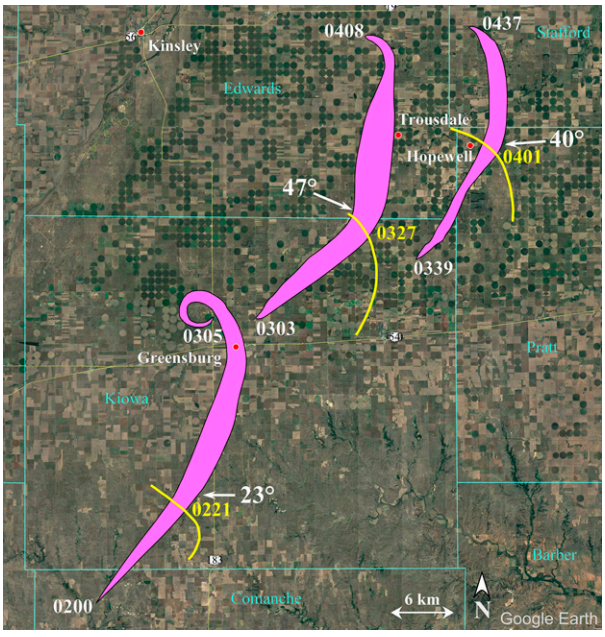

FIG. 18. Damage paths and start/end times of the Greensburg, Trousdale, and Hopewell, KS, tornadoes occurring between 0200 and 0437 UTC 5 May 2007. Tornado midlife heading changes indicated along with RFISB locations (yellow lines) analyzed from KDDC 0.5° radial velocity at a time closest to the turn midpoint (yellow; UTC). Damage paths and dimensions are as presented in Lemon and Umscheid (2008).

resolved and observer reports are not available. Momentum directionality within the major surges favored marked leftward tornado heading changes; however, tornadoes can take rightward turns related to RF outflow-associated changes as evidenced in the short rightward HT track segments, and as documented in Marquis et al. (2012) and French et al. (2014). From the cases analyzed and others previously cited, changes in tornado heading and speed appear to be related to the 1) size, magnitude, and directionality of the internal-surge momentum, and 2) evolution of the tornado-relative position of the surge core (i.e., evolving directionality).

Both the Nixon and Allen (2021) results and those presented herein emphasize leftward tornado heading changes. Our study highlights the role RFISs play in altering the tornado-proximate outflow versus inflow momentum balance, including momentum directionality evolution, that results in tornado heading and speed changes. A key related facet of the Nixon and Allen study is the tornado advective role played by the environmental mean wind in the 0–500-m layer. To an appreciable degree, it is this low-level flow that substantially contributes to the inflow part of the proximate momentum balance in the tornadic region of the supercell. Stronger inflow not balanced by storm outflow should lead to leftward/rearward storm-relative motion consistent with DB02. Given the abrupt nature by which intense RFISs may alter the bounding flow field near tornadoes, we would anticipate that the tornado heading changes, in general, would occur over a substantially shorter period than those in Nixon and Allen's study.

Effective RFIS monitoring is a function of radar-relative storm proximity and azimuthal location. Based on our experience examining numerous RFISs in radar data, most substantial surges can be identified and tracked within 75 km of a WSR-88D at 0.5° tilt given the ~1 km ARL beam height at that range and assuming the flow field motion is not largely orthogonal to the beam. Expanding this perimeter to 100 km would still include many RF outflows with a depth of at least 1.5 km. For supercells residing outside this approximate range or where the sensing angle constrains RFIS sampling, the storm-relative hook echo tip motion can signal a major RF momentum change.

With just a few cases presented here and in past research, further studies of the relationship between major RFISs and tornado motion changes are needed. In the course of looking at other events, we conclude this paper with a compelling example, the high-profile tornadic "Greensburg" supercell of 4 May 2007 (Lemon and Umscheid 2008; Bluestein 2009; Tanamachi et al. 2012). This event featured several particularly large tornadoes that underwent a substantial heading change well after genesis (>20 min), but long before the onset of the dissipation phase. Tracks for the three largest tornadoes (Greensburg, Trousdale, Hopewell) are shown in Fig. 18. The largest midlife track change (47°) occurred with the extremely wide Trousdale tornado (maximum width of 4.1 km). Most relevant was that each of these marked tornado track changes was accompanied by a major RFIS (Fig. 18). We are investigating how often substantial track changes of significant tornadoes are temporally associated with major RFISs.

Acknowledgments. This research was supported by the National Science Foundation under Grant AGS-1832326. Our research has benefitted substantially from numerous conversations with Patrick Skinner regarding supercell rear-flank surges and other related topics. Skip Talbot generously provided MPAR graphics of the El Reno event. We are appreciative of the dedicated efforts of the TWISTEX crews in the challenging Quinter deployment. Chris Collura, Doug Kiesling, and Jennifer Brindley Ubl kindly contributed videographic or photographic materials for this research. The ERT center locations in 1-min intervals as reported in NOAA (2014) were produced by Gabe Garfield and Jeff Snyder from analysis of RaXPol and KTLX radar data.

Data availability statement. WSR-88D Level II data analyzed in this study are publicly available from the Next Generation Weather Radar repository located on Amazon Web Services at https://s3.amazonaws.com/noaa-nexrad-level2/index.html. Videography and accompanying MPAR and KTLX underlay imagery for the 31 May 2013 ERT event is available within the TED (Seimon et al. 2016) at http://el-reno-survey.net/ted.

REFERENCES

Adlerman, E. J., K. K. Droegemeier, and R. Davies-Jones, 1999: A numerical simulation of cyclic mesocyclogenesis. *J. Atmos.*

Sci., **56**, 2045–2069, https://doi.org/10.1175/1520-0469(1999)056<2045:ANSOCM>2.0.CO;2.

Agee, E., J. Snow, and P. Clare, 1976: Multiple vortex features in the tornado cyclone and the occurrence of tornado families. *Mon. Wea. Rev.*, **104**, 552–563, https://doi.org/10.1175/1520-0493(1976)104<0552:MVFITT>2.0.CO;2.

Beck, J. R., J. L. Schroeder, and J. M. Wurman, 2006: High-resolution dual-Doppler analysis of the 29 May 2001 Kress, Texas, cyclic supercell. *Mon. Wea. Rev.*, **134**, 3125–3148, https://doi.org/10.1175/MWR3246.1.

Bluestein, H. B., 2009: The formation and early evolution of the Greensburg, Kansas, tornadic supercell on 4 May 2007. *Wea. Forecasting*, **24**, 899–920, https://doi.org/10.1175/2009WAF2222206.1.

——, C. C. Weiss, and A. L. Pazmany, 2004: The vertical structure of a tornado near Happy, Texas, on 5 May 2002: High-resolution, mobile, W-band, Doppler radar observations. *Mon. Wea. Rev.*, **132**, 2325–2337, https://doi.org/10.1175/1520-0493(2004)132<2325:TVSOAT>2.0.CO;2.

——, ——, M. M. French, E. M. Holthaus, R. L. Tanamachi, S. Frasier, and A. L. Pazmany, 2007: The structure of tornadoes near Attica, Kansas, on 12 May 2004: High-resolution, mobile, Doppler radar observations. *Mon. Wea. Rev.*, **135**, 475–506, https://doi.org/10.1175/MWR3295.1.

——, J. C. Snyder, and J. B. Houser, 2015: A multiscale overview of the El Reno, Oklahoma, tornadic supercell of 31 May 2013. *Wea. Forecasting*, **30**, 525–552, https://doi.org/10.1175/WAF-D-14-00152.1.

——, K. J. Thiem, J. C. Snyder, and J. B. Houser, 2018: The multiple-vortex structure of the El Reno, Oklahoma, tornado on 31 May 2013. *Mon. Wea. Rev.*, **146**, 2483–2502, https://doi.org/10.1175/MWR-D-18-0073.1.

Brandes, E. A., 1978: Mesocyclone evolution and tornadogenesis: Some observations. *Mon. Wea. Rev.*, **106**, 995–1011, https://doi.org/10.1175/1520-0493(1978)106<0995:MEATSO>2.0.CO;2.

Burgess, D. W., V. T. Wood, and R. A. Brown, 1982: Mesocyclone evolution statistics. *12th Conf. on Severe Local Storms*, San Antonio, TX, Amer. Meteor. Soc., 422–424.

Chrisman, J. N., 2013: Dynamic scanning. *NEXRAD Now*, No. 22, WSR-88D Radar Operations Center, Norman, OK, 1–3, https://www.roc.noaa.gov/WSR88D/PublicDocs/NNOW/NNow22c.pdf.

——, 2014: Multiple elevation scan option for SAILS (MESO-SAILS)—The next step in dynamic scanning for the WSR-88D. WSR-88D Radar Operations Center, 27 pp., https://www.roc.noaa.gov/WSR88D/PublicDocs/NewTechnology/MESO-SAILS_Description_Briefing_Jan_2014.pdf.

Coffer, B. E., and M. D. Parker, 2017: Simulated supercells in nontornadic and tornadic VORTEX2 environments. *Mon. Wea. Rev.*, **145**, 149–180, https://doi.org/10.1175/MWR-D-16-0226.1.

Davies-Jones, R. P., and H. E. Brooks, 1993: Mesocyclogenesis from a theoretical perspective. *The Tornado: Its Structure, Dynamics, Prediction, and Hazards, Geophys. Monogr.*, Vol. 79, Amer. Geophys. Union, 105–114, https://doi.org/10.1029/GM079p0105.

——, C. A. Doswell, D. W. Burgess, and J. F. Weaver, 1994: Some noteworthy aspects of the Hesston, Kansas, tornado family of 13 March 1990. *Bull. Amer. Meteor. Soc.*, **75**, 1007–1017, https://doi.org/10.1175/1520-0477(1994)075<1007:SNAOTH>2.0.CO;2.

Dowell, D. C., and H. B. Bluestein, 2002: The 8 June 1995 McLean, Texas, storm. Part II: Cyclic tornado formation, maintenance, and dissipation. *Mon. Wea. Rev.*, **130**, 2649–2670, https://doi.org/10.1175/1520-0493(2002)130<2649:TJMTSP>2.0.CO;2.

Finley, C. A., and B. D. Lee, 2004: High resolution mobile mesonet observations of RFD surges in the June 9 Basset, Nebraska supercell during Project ANSWERS 2003. *22nd Conf. on Severe Local Storms*, Hyannis, MA, Amer. Meteor. Soc., P11.3, https://ams.confex.com/ams/11aram22sls/webprogram/Paper82005.html.

——, and ——, 2008: Mobile mesonet observations of an intense RFD and multiple RFD gust fronts in the May 23 Quinter, Kansas tornadic supercell during TWISTEX 2008. *24th Conf. on Severe Local Storms*, Savannah, GA, Amer. Meteor. Soc., P3.18, https://ams.confex.com/ams/24SLS/techprogram/paper_142133.htm.

——, L. Orf, B. D. Lee, and R. B. Wilhelmson, 2018: High-resolution simulation of a violent tornado in the 27 April 2011 outbreak environment. *29th Conf. on Severe Local Storms*, Stowe, VT, Amer. Meteor. Soc., 10B.5, https://ams.confex.com/ams/29SLS/webprogram/Paper348812.html.

French, M. M., and D. M. Kingfield, 2019: Dissipation characteristics of tornado vortex signatures associated with long-duration tornadoes. *J. Appl. Meteor. Climatol.*, **58**, 317–339, https://doi.org/10.1175/JAMC-D-18-0187.1.

——, H. B. Bluestein, I. PopStefanija, C. A. Baldi, and R. T. Bluch, 2014: Mobile, phased-array, Doppler radar observations of tornadoes at X band. *Mon. Wea. Rev.*, **142**, 1010–1036, https://doi.org/10.1175/MWR-D-13-00101.1.

——, P. S. Skinner, L. J. Wicker, and H. B. Bluestein, 2015: Documenting a rare tornado merger observed in the 24 May 2011 El Reno–Piedmont, Oklahoma, supercell. *Mon. Wea. Rev.*, **143**, 3025–3043, https://doi.org/10.1175/MWR-D-14-00349.1.

Fujita, T. T., 1981: Tornadoes and downbursts in the context of generalized planetary scales. *J. Atmos. Sci.*, **38**, 1511–1534, https://doi.org/10.1175/1520-0469(1981)038<1511:TADITC>2.0.CO;2.

——, 1992: *Memoirs of an Effort to Unlock the Mystery of Severe Storms during the 50 Years, 1942–1992*. University of Chicago, 298 pp.

Grzych, M. L., B. D. Lee, and C. A. Finley, 2007: Thermodynamic analysis of supercell rear-flank downdrafts from project ANSWERS. *Mon. Wea. Rev.*, **135**, 240–246, https://doi.org/10.1175/MWR3288.1.

Hargrove, B., 2018: *The Man Who Caught the Storm*. Simon & Schuster, 296 pp.

Heinselman, P. L., and S. M. Torres, 2011: High-temporal-resolution capabilities of the National Weather Radar Testbed Phased-Array Radar. *J. Appl. Meteor. Climatol.*, **50**, 579–593, https://doi.org/10.1175/2010JAMC2588.1.

——, D. L. Priegnitz, K. L. Manross, T. M. Smith, and R. W. Adams, 2008: Rapid sampling of severe storms by the National Weather Radar testbed phased array radar. *Wea. Forecasting*, **23**, 808–824, https://doi.org/10.1175/2008WAF2007071.1.

Hirth, B. D., J. L. Schroeder, and C. C. Weiss, 2008: Surface analysis of the rear-flank downdraft outflow in two tornadic supercells. *Mon. Wea. Rev.*, **136**, 2344–2363, https://doi.org/10.1175/2007MWR2285.1.

Houser, J. L., H. B. Bluestein, and J. C. Snyder, 2015: Rapid-scan, polarimetric, Doppler radar observations of tornadogenesis and tornado dissipation in a tornadic supercell: The "El Reno, Oklahoma" storm of 24 May 2011. *Mon. Wea. Rev.*, **143**, 2685–2710, https://doi.org/10.1175/MWR-D-14-00253.1.

Jensen, B., E. N. Rasmussen, T. P. Marshall, and M. A. Mabey, 1983: Storm scale structure of the Pampa storm. *13th Conf. on Severe Local Storms*, Tulsa, OK, Amer. Meteor. Soc., 85–88.

Karstens, C. D., T. M. Samaras, B. D. Lee, W. A. Gallus, and C. A. Finley, 2010: Near-ground pressure and wind measurements in tornadoes. *Mon. Wea. Rev.*, **138**, 2570–2588, https://doi.org/10.1175/2010MWR3201.1.

Klemp, J. B., and R. Rotunno, 1983: A study of the tornadic region within a supercell thunderstorm. *J. Atmos. Sci.*, **40**, 359–377, https://doi.org/10.1175/1520-0469(1983)040<0359:ASOTTR>2.0.CO;2.

Kosiba, K., J. Wurman, Y. Richardson, P. Markowski, P. Robinson, and J. Marquis, 2013: Genesis of the Goshen County, Wyoming, tornado on 5 June 2009 during VORTEX2. *Mon. Wea. Rev.*, **141**, 1157–1180, https://doi.org/10.1175/MWR-D-12-00056.1.

Kumjian, M. R., and A. D. Schenkman, 2008: Interpretation of the "flying eagle" radar signature in supercells. *24th Conf. on Severe Local Storms*, Savannah, GA, Amer. Meteor. Soc. P14.2, https://ams.confex.com/ams/pdfpapers/141917.pdf.

——, and A. V. Ryzhkov, 2008: Polarimetric signatures in supercell thunderstorms. *J. Appl. Meteor. Climatol.*, **47**, 1940–1961, https://doi.org/10.1175/2007JAMC1874.1.

Kurdzo, J. M., D. J. Bodine, B. L. Cheong, and R. D. Palmer, 2015: High-temporal resolution polarimetric X-band Doppler radar observations of the 20 May 2013 Moore, Oklahoma, tornado. *Mon. Wea. Rev.*, **143**, 2711–2735, https://doi.org/10.1175/MWR-D-14-00357.1.

Lee, B. D., C. A. Finley, and P. S. Skinner, 2004: Thermodynamic and kinematic analysis of multiple RFD surges for the 24 June 2003 Manchester, SD, cyclic tornadic supercell during Project ANSWERS 2003. *22nd Conf. on Severe Local Storms*, Hyannis, MA, Amer. Meteor. Soc., P11.2, https://ams.confex.com/ams/11aram22sls/webprogram/Paper82000.html.

——, ——, C. D. Karstens, and T. M. Samaras, 2010: Surface observations of the rear-flank downdraft evolution associated with the Aurora, NE tornado of 17 June 2009. *25th Conf. on Severe Local Storms,* Denver, CO, Amer. Meteor. Soc., P8.27, https://ams.confex.com/ams/25SLS/webprogram/Paper176133.html.

——, ——, and T. M. Samaras, 2011: Surface analysis near and within the Tipton, Kansas, tornado on 29 May 2008. *Mon. Wea. Rev.*, **139**, 370–386, https://doi.org/10.1175/2010MWR3454.1.

——, ——, and C. D. Karstens, 2012: The Bowdle, South Dakota, cyclic tornadic supercell of 22 May 2010: Surface analysis of rear-flank downdraft evolution and multiple internal surges. *Mon. Wea. Rev.*, **140**, 3419–3441, https://doi.org/10.1175/MWR-D-11-00351.1.

Lemon, L. R., and M. Umscheid, 2008: The Greensburg, Kansas tornadic storm: A storm of extremes. *24th Conf. on Severe Local Storms*, Savannah, GA, Amer. Meteor. Soc., 2.4, http://ams.confex.com/ams/pdfpapers/141811.pdf.

Magsig, M. A., and M. D. Austin, 2014: An evaluation of the potential impact of SAILS on the warning decision making of the 31 May 2013 El Reno, OK storm. *27th Conf. on Severe Local Storms*, Madison, WI, Amer. Meteor. Soc., 36, https://ams.confex.com/ams/27SLS/webprogram/Paper255909.html.

Markowski, P. M., and Y. Richardson, 2009: Tornadogenesis: Our current understanding, forecasting considerations, and questions to guide future research. *Atmos. Res.*, **93**, 3–10, https://doi.org/10.1016/j.atmosres.2008.09.015.

——, and ——, 2014: The influence of environmental low-level shear and cold pools on tornadogenesis: Insights from idealized simulations. *J. Atmos. Sci.*, **71**, 243–275, https://doi.org/10.1175/JAS-D-13-0159.1.

——, J. M. Straka, and E. N. Rasmussen, 2002: Direct surface thermodynamic observations within the rear-flank downdrafts of nontornadic and tornadic supercells. *Mon. Wea. Rev.*, **130**, 1692–1721, https://doi.org/10.1175/1520-0493(2002)130<1692:DSTOWT>2.0.CO;2.

——, and Coauthors, 2012: The pretornadic phase of the Goshen County, Wyoming, supercell of 5 June 2009 intercepted by VORTEX 2. Part II: Intensification of low-level rotation. *Mon. Wea. Rev.*, **140**, 2916–2938, https://doi.org/10.1175/MWR-D-11-00337.1.

Marquis, J., Y. Richardson, P. Markowski, D. Dowell, and J. Wurman, 2012: Tornado maintenance investigated with high-resolution dual-Doppler and EnKF analysis. *Mon. Wea. Rev.*, **140**, 3–27, https://doi.org/10.1175/MWR-D-11-00025.1.

NCDC, 2008: *Storm Data*. Vol. 50, No. 5, National Climatic Data Center, Asheville, NC, 622 pp.

——, 2013: *Storm Data*. Vol. 55, No. 5, National Climatic Data Center, Asheville, NC, 684 pp.

——, 2017: *Storm Data*. Vol. 59, No. 7, National Climatic Data Center, Asheville, NC, 789 pp.

Nielson, E. R., and R. S. Schumacher, 2020: Dynamical mechanisms supporting extreme rainfall accumulations in the Houston "Tax Day" 2016 flood. *Mon. Wea. Rev.*, **148**, 83–109, https://doi.org/10.1175/MWR-D-19-0206.1.

Nixon, C. J., and J. T. Allen, 2021: Anticipating deviant tornado motion using a simple hodograph technique. *Wea. Forecasting*, **36**, 219–235, https://doi.org/10.1175/WAF-D-20-0056.1.

NOAA, 2014: Service assessment: May 2013 Oklahoma tornadoes and flash flooding. National Weather Service, 42 pp. + appendixes, https://www.weather.gov/media/publications/assessments/13oklahoma_tornadoes.pdf.

Orf, L., R. Wilhelmson, B. Lee, C. Finley, and A. Houston, 2017: Evolution of a long-track, violent tornado in a simulated supercell. *Bull. Amer. Meteor. Soc.*, **98**, 45–68, https://doi.org/10.1175/BAMS-D-15-00073.1.

Pazmany, A. L., J. B. Mead, H. B. Bluestein, J. C. Snyder, and J. B. Houser, 2013: A mobile, rapid-scanning, X-band, polarimetric (RaXPol) Doppler-radar system. *J. Atmos. Oceanic Technol.*, **30**, 1398–1413, https://doi.org/10.1175/JTECH-D-12-00166.1.

Pecos Hank, 2020: Fastest moving tornado—New World Record. *YouTube*, Accessed 1 March 2021, https://www.youtube.com/watch?v=gMws8ueXJ7U.

Richardson, Y. P., P. Markowski, J. N. Marquis, J. Wurman, K. A. Kosiba, P. Robinson, D. W. Burgess, and C. C. Weiss, 2012: Tornado maintenance and demise in the Goshen County, Wyoming supercell of 5 June 2009 intercepted by VORTEX2. *26th Conf. on Severe Local Storms*, Nashville, TN, Amer. Meteor. Soc., 13.3, https://ams.confex.com/ams/26SLS/webprogram/Paper212526.html.

Riganti, C. J., and A. L. Houston, 2017: Rear-flank outflow dynamics and thermodynamics in the 10 June 2010 Last Chance, Colorado, supercell. *Mon. Wea. Rev.*, **145**, 2487–2504, https://doi.org/10.1175/MWR-D-16-0128.1.

Ryzhkov, A. V., T. J. Schuur, D. W. Burgess, and D. S. Zrnić, 2005: Polarimetric tornado detection. *J. Appl. Meteor.*, **44**, 557–570, https://doi.org/10.1175/JAM2235.1.

Schenkman, A. D., M. Xue, and D. T. Dawson II, 2016: The cause of internal outflow surges in a high-resolution simulation of the 8 May 2003 Oklahoma City tornadic supercell. *J. Atmos. Sci.*, **73**, 353–370, https://doi.org/10.1175/JAS-D-15-0112.1.

Seimon, A., J. T. Allen, T. A. Seimon, S. J. Talbot, and D. K. Hoadley, 2016: Crowdsourcing the El Reno 2013 tornado: A new approach for collation and display of storm chaser imagery for scientific applications. *Bull.*

Amer. Meteor. Soc., **97**, 2069–2084, https://doi.org/10.1175/BAMS-D-15-00174.1.

Skinner, P. S., C. C. Weiss, J. L. Schroeder, L. J. Wicker, and M. I. Biggerstaff, 2011: Observations of the surface boundary structure within the 23 May 2007 Perryton, Texas, supercell. *Mon. Wea. Rev.*, **139**, 3730–3749, https://doi.org/10.1175/MWR-D-10-05078.1.

——, ——, M. M. French, H. B. Bluestein, P. M. Markowski, and Y. P. Richardson, 2014: VORTEX2 observations of a low-level mesocyclone with multiple internal rear-flank downdraft momentum surges in the 18 May 2010 Dumas, Texas, supercell. *Mon. Wea. Rev.*, **142**, 2935–2960, https://doi.org/10.1175/MWR-D-13-00240.1.

——, ——, L. J. Wicker, C. K. Potvin, and D. C. Dowell, 2015: Forcing mechanisms for an internal rear-flank downdraft momentum surge in the 18 May 2010 Dumas, TX, supercell. *Mon. Wea. Rev.*, **143**, 4305–4330, https://doi.org/10.1175/MWR-D-15-0164.1.

Skow, K. D., and C. Cogil, 2017: High-resolution aerial survey and radar analysis of quasi-linear convective system surface vortex damage paths from 31 August 2014. *Wea. Forecasting*, **32**, 441–467, https://doi.org/10.1175/WAF-D-16-0136.1.

Snyder, J. C., and H. B. Bluestein, 2014: Some considerations for the use of high-resolution mobile radar data in tornado intensity determination. *Wea. Forecasting*, **29**, 799–827, https://doi.org/10.1175/WAF-D-14-00026.1.

Tanamachi, R. L., H. B. Bluestein, J. B. Houser, S. J. Frasier, and K. M. Hardwick, 2012: Mobile, X-band, polarimetric Doppler radar observations of the 4 May 2007 Greensburg, Kansas, tornadic supercell. *Mon. Wea. Rev.*, **140**, 2103–2125, https://doi.org/10.1175/MWR-D-11-00142.1.

Umscheid, M., 2007: May 5, 2007: A "career storm"—Greensburg, KS. Accessed 18 March 2021, http://www.underthemeso.com/blog/?p=364.

——, and J. Hutton, 2008: A state record tornado outbreak: Preliminary investigation of 23 May 2008 supercells and tornadoes. NOAA, 31 pp., https://www.deepconvection.com/12HPC/presentations/Mike%20Umscheid-2008May23.pdf.

Wakimoto, R. M., 2011: The LaGrange tornado during VORTEX2. Part I: Photogrammetric analysis of the tornado combined with single-Doppler radar data. *Mon. Wea. Rev.*, **139**, 2233–2258, https://doi.org/10.1175/2010MWR3568.1.

——, and B. E. Martner, 1992: Observations of a Colorado tornado. Part II: Combined photogrammetric and Doppler radar analysis. *Mon. Wea. Rev.*, **120**, 522–543, https://doi.org/10.1175/1520-0493(1992)120<0522:OOACTP>2.0.CO;2.

——, H. V. Murphey, D. C. Dowell, and H. B. Bluestein, 2003: The Kellerville tornado during VORTEX: Damage survey and Doppler radar analysis. *Mon. Wea. Rev.*, **131**, 2197–2221, https://doi.org/10.1175/1520-0493(2003)131<2197:TKTDVD>2.0.CO;2.

——, and Coauthors, 2016: Aerial damage survey of the 2013 El Reno tornado combined with mobile radar data. *Mon. Wea. Rev.*, **144**, 1749–1776, https://doi.org/10.1175/MWR-D-15-0367.1.

Weadon, M., P. Heinselman, D. Forsyth, W. E. Benner, G. S. Torok, and J. Kimpel, 2009: Multifunction phased array radar. *Bull. Amer. Meteor. Soc.*, **90**, 385–389, https://doi.org/10.1175/2008BAMS2666.1.

Weiss, C., D. C. Dowell, J. L. Schroeder, P. S. Skinner, A. E. Reinhart, P. M. Markowski, and Y. P. Richardson, 2015: A comparison of near-surface buoyancy and baroclinity across three VORTEX2 supercell intercepts. *Mon. Wea. Rev.*, **143**, 2736–2753, https://doi.org/10.1175/MWR-D-14-00307.1.

Wicker, L. J., and R. B. Wilhelmson, 1995: Simulation and analysis of tornado development and decay within a three-dimensional supercell thunderstorm. *J. Atmos. Sci.*, **52**, 2675–2703, https://doi.org/10.1175/1520-0469(1995)052<2675:SAAOTD>2.0.CO;2.

Wurman, J., and S. Gill, 2000: Finescale radar observations of the Dimmitt, Texas (2 June 1995), tornado. *Mon. Wea. Rev.*, **128**, 2135–2164, https://doi.org/10.1175/1520-0493(2000)128<2135:FROOTD>2.0.CO;2.

——, and K. Kosiba, 2013: Finescale radar observations of tornado and mesocyclone structures. *Wea. Forecasting*, **28**, 1157–1174, https://doi.org/10.1175/WAF-D-12-00127.1.

——, Y. Richardson, C. Alexander, S. Weygandt, and P. F. Zhang, 2007: Dual-Doppler and single-Doppler analysis of a tornadic storm undergoing mergers and repeated tornadogenesis. *Mon. Wea. Rev.*, **135**, 736–758, https://doi.org/10.1175/MWR3276.1.

——, K. Kosiba, P. Markowski, Y. Richardson, D. Dowell, and P. Robinson, 2010: Finescale single- and dual-Doppler analysis of tornado intensification, maintenance, and dissipation in the Orleans, Nebraska, supercell. *Mon. Wea. Rev.*, **138**, 4439–4455, https://doi.org/10.1175/2010MWR3330.1.

——, ——, P. Robinson, and T. Marshall, 2014: The role of multiple-vortex tornado structure in causing storm researcher fatalities. *Bull. Amer. Meteor. Soc.*, **95**, 31–45, https://doi.org/10.1175/BAMS-D-13-00221.1.

Zrnić, D. S., and Coauthors, 2007: Agile-beam phased array radar for weather observations. *Bull. Amer. Meteor. Soc.*, **88**, 1753–1766, https://doi.org/10.1175/BAMS-88-11-1753.